BIOMECHANICALLY-REGULARIZED DEFORMABLE IMAGE REGISTRATION FOR HEAD AND NECK ADAPTIVE RADIATION THERAPY

by

Jihun Kim

A dissertation submitted in partial fulfillment
of the requirements for the degree of
Doctor of Philosophy
(Mechanical Engineering)
in The University of Michigan
2015

Doctoral Committee:

Professor Kazuhiro Saitou, Co-Chair
Professor James M. Balter, Co-Chair
Professor James Ashton-Miller
Assistant Professor Martha M. Matuszak

TABLE OF CONTENTS

LIST OF TABLES

TABLE

LIST OF FIGURES

FIGURE

ABSTRACT

Radiation treatment (RT) is an established method of treating head and neck (HN) cancer, 3 percent of all cancers in the United States, by delivering conformal radiation dose to tumors while sparing surrounding healthy tissue. However, tumors (and healthy tissue) that change in shape and location during the 5-7 weeks of RT may not be sufficiently covered (and spared) by the initial radiation treatment plan, which is planned on a regular computed tomography (CT) scan (high-resolution and wide-view) taken prior to the start of RT. To monitor during-RT changes, a HN cancer patient may be scanned using a cone-beam CT scanner (CBCT, low-resolution and narrow-view) at every treatment fraction. In HN adaptive radiation therapy, the during-RT changes that can be detected by using the daily CBCT images may be further utilized to adjust the initial radiation treatment plan to prevent insufficient radiation dose to the tumors and excessive radiation dose to the healthy tissue.

B-spline deformable image registration (DIR) is an important tool for RT for computing the deformations (represented as a linear combination of B-spline functions) between the regular CT and the CBCT images for the HN patient (i.e. the deformation of the tumors and surrounding healthy tissue). However, the B-spline DIR, which is formulated as an optimization problem to find a deformation map that simply maximizes a similarity metric between two images, may result in physically unreasonable deformations, such as bone warping. In particular, existing approaches, which penalize non-orthonormality of the deformation gradient tensor during optimization, cannot fully prevent the warping in multiple rigid bodies in close proximity (e.g., cervical vertebrae in the HN region). In addition, the B-spline DIR may fail to obtain an accurate deformation of soft tissue depending on the selection of registration parameters. Finally, the previous studies have evaluated the registration accuracy with a limited number of landmarks, with which the accuracy of the volumetric deformation cannot be rigorously evaluated.

The objective of this dissertation is 1) to improve the registration accuracy of HN CT images by introducing penalty terms into the B-spline DIR derived from physical principles, and

2) to develop an improved evaluation method for the registration accuracy based on the finite element model (FE) model of HN regions.

First, a penalty for preventing deformations in rigid regions (bones) was developed. It was designed to preserve inter-voxel distances within each of the rigid regions. It outperformed an existing penalty for cases of B-spline DIR of five cervical vertebrae in the HN region, where multiple skeletal elements exist in close proximity.

Second, another penalty for preventing non-physical deformations in soft tissues was developed. It was designed to prevent the resultant deformations from violating the partial differential equations for linear elastic material. The penalty corrected large misalignments, which resulted from the B-spline DIR without the penalty and under some of the parametric settings associated with the image metric and optimization algorithm used.

Third, a FE model of the HN region including five cervical vertebrae was developed as a tool for the evaluation of registration accuracy. The surrounding tissue was assumed as homogeneous, linear elastic material. The displacement boundary conditions were obtained for the bony elements by aligning the corresponding surface structures. The FE model generated the deformation maps similar to those seen in patients, which may be used as ground-truth for the evaluation of registration accuracy.

The outcome of the dissertation would support research/development in adaptive radiation treatment of head and neck cancer by enabling the accurate estimation of deformations of healthy tissue surrounding tumor and the rigorous assessment of registration accuracy.

Chapter 1. Introduction

1.1 Background

Radiation treatment (RT) is an established method of treating head and neck (HN) cancer, which account for approximately 3 percent of all cancers in the United States [1]. Advanced RT techniques such as intensity-modulated radiation therapy (IMRT) [2] have enhanced treatment outcomes by delivering conformal radiation dose to tumors while sparing healthy surrounding tissues.

However, the RT quality of HN cancer may be deteriorated because the tumors and the healthy surrounding tissues change in shape and location during 5-7 weeks of RT. Due to this change, the tumors may be radiated by insufficient dose and the healthy tissues by excessive dose when the radiation dose is planned on the patient image taken prior to the start of RT—the planning image, taken using a regular computed tomography (CT) scanner (high-resolution and wide-view)—and is not adjusted. Barker *et al.* reported that the volumes of a tumor and a parotid gland decreased at median rates of 1.7−1.8 %/day and 0.6 %/day in a study with 14 HN cancer patients [3]. Lee *et al.* reported that the parotid glands of 10 HN patients migrated toward the center of patient body (possibly toward a region of high radiation dose) with a median rate of 0.22 mm/day in addition to the volume decrease (a median rate of 0.7 %/day) [4]. The impact of the geometric change of parotid glands on the radiation dose delivered to HN patients was

investigated in Lee *et al.*, reporting that 3 of 10 patients received unexpectedly high exposure to radiation, which was 13−42 % higher than planned [5].

In order to overcome this difficulty, adaptive radiation therapy (ART) has gathered strong interest during the past few decades because it has a potential to better treat cancer patients by adjusting the radiation dose in response to the deformations in the tumors and healthy surrounding tissues. As an example of ART, a HN patient may be scanned at every treatment fraction using a cone-beam CT (CBCT) scanner (low-resolution and narrow-view) to monitor the deformations in the tumors and healthy surrounding tissues. These additional CBCT scans (treatment CT images) may be further used via the following procedures: (1) defining contours of the tumors and healthy surrounding tissues, (2) calculating the radiation dose delivered to the patient and the total accumulated radiation dose, and (3) determining whether/how the radiation dose planned on the planning image in response to the deformations seen in the treatment images. However, it is extremely time-consuming for physicians to manually delineate the contours at every treatment scans. In addition, calculating the accumulated radiation dose requires a geometric mapping (or a deformation map) from the planning CT image to the treatment CT images.

Therefore, deformable image registration (DIR) is an important tool for RT for computing the deformation maps between the planning CT and treatment CT images for a HN patient. Using the voxel-by-voxel deformation maps by DIR, the aforementioned procedures in ART can be automated. First, the contours delineated on the planning CT image can be transformed to the treatment CT images by using the resultant deformation maps by DIR [4, 6-

7]. Second, the radiation doses calculated on each treatment CT image can be transformed to the coordinates of the planning CT image, resulting in the accumulated radiation dose. [6, 8-9] For instance, in a retrospective study [5], Lee *et al.* used a DIR algorithm for the automatic contouring of parotid glands and the dose accumulation to calculate the radiation dose delivered to the parotid glands.

1.2 Motivation

B-spline DIR, which is one of the most popular DIR methods and in which deformation is represented as a linear combination of B-spline basis functions, is formulated as an optimization problem to find a deformation that simply maximizes an image similarity metric from one image (reference) to another (target). In a recent study [10], it was found that image similarity metrics, such as root mean squares, normalized cross correlation, and normalized mutual information, cannot be reliable surrogates for the registration accuracy. Therefore, B-spline DIR often results in physically unreasonable deformations such as born warping.

In addition, it has been reported that many of existing DIR algorithms including B-spline DIR resulted in large errors [11]. A multi-institute evaluation study reported that maximum errors ranged from 5.1 to 15.4 mm for several DIR techniques in Kashani *et al*. For HN images, a recent work [12] reported a registration error of 3.3 mm for a B-spline DIR. Kirby *et al.* developed a two-dimensional deformable phantom to quantitatively verify B-spline DIR algorithms. In this previous study [13], it was found that the B-spline DIR algorithms with four

different intensity metrics (cross correlation, mutual information, sum of absolute differences, and sum of squared difference) resulted in at least 3 mm registration error for 24-25 of the 32 points, at which the registration errors were estimated.

Furthermore, evaluating the accuracy of deformable image registration is also challenging. This is because a true deformation is not given with the images. Many previous works [12, 14-15] used target registration error calculated based on landmark pairs. However, the target registration errors calculated using a limited number of landmark pairs may not exactly reflect the accuracy of the volumetric deformations.

1.3 Objective

The objective of this thesis is (1) to develop penalty terms to improve the accuracy of the B-spline DIR of HN CT images, and (2) to develop a finite element (FE) model that can be used to evaluate registration accuracy.

The problems which will be addressed in this thesis are as follows:

- B-spline DIR may result in physically unreasonable deformation, such was bone warping, without further guidance by penalty terms. How can the accuracy of the B-spline DIR of the HN CT images be improved?
- There has not been a reliable gold standard, with which to evaluate the accuracy of the B-spline DIR of the HN CT images. How can the accuracy of the B-spline DIR be rigorously evaluated?

In order to improve the accuracy of the B-spline DIR in the HN region, penalty terms were designed to preserve physical behaviors anticipated for bony structures and soft tissues. The development of a penalty for the B-spline DIR of five cervical vertebrae was based on the fundamental fact that a distance between any points within a rigid body should remain the same before and after deformation. For the B-spline DIR of soft tissue, a penalty was designed to prevent the resultant deformations in the soft tissue region from violating the static equilibrium equations for linear elastic materials.

Moreover, FE HN models were constructed based on HN CT images. The FE model is capable of generating physically realistic deformation maps, such as no local deformation in bony structures, under appropriate boundary conditions. In a FE-based evaluation framework, a set of the deformation computed by using the FE models and synthetically-computed images can establish an evaluation tool of registration accuracy—image data sets and corresponding ground-truth deformation.

1.4 Thesis Outline

The next chapter discusses the previous studies related to the development of the penalty terms for deformable image registration. Chapter 2 introduces penalty terms that were designed to preserve rigidity and linear elasticity. In addition, some previous studies on the evaluation of deformable image registration accuracy will be discussed in Chapter 2.

Chapter 3 discusses a penalty developed in order to improve the accuracy of the B-spline DIR of bony elements in the HN region. In Chapter 3, it will be described how the penalty was formulated. By testing the B-spline DIR on 25 image pairs of HN CT images, the impact of the penalty was investigated compared to the DIR without a penalty and with an existing penalty.

Chapter 4 describes a penalty developed to preserve linear elasticity in soft tissue when B-spline DIR is performed in the HN region. In Chapter 4, it will be described how the penalty was derived from the fundamental theory of solid mechanics. The accuracy of aligning a muscle in neck, sternocleidomastoid, was evaluated by performing the DIR on HN CT images. It will be also discussed how the developed penalty can improve the accuracy of the B-spline DIR across the selection of registration parameters.

In Chapter 5, a FE-based evaluation method will be discussed. Chapter 5 discusses the ability of the FE models to generate deformation maps similar to the ones seen between HN CT images. The FE model was used to evaluate the accuracy of the B-spline DIR of five cervical vertebrae in the HN region. The registration results, which had a similar trend with those presented in Chapter 3, showed that the FE models can be used as a tool for the accuracy evaluation of B-spline DIR algorithms.

Chapter 6 discusses limitations of this thesis and suggests several future studies. Finally, the contributions of the thesis will be discussed in Chapter 6.

Chapter 2. Related Work

2.1 Penalty for Deformable Image Registration

In order to prevent non-physical deformation maps, there have been efforts to use mathematical or biomechanical penalties or constraints within deformable image registration (DIR), which is formulated as an optimization problem to find a deformation map that maximizes a similarity metric between two images. Sorzano *et al.* developed a mathematical penalty term by using the divergence and curl of the deformation to enhance its smoothness [16]. Sdika proposed constraints on the Jacobian of deformations and its derivatives in order to prevent noninvertible transformation [17]. Rohlfing *et al*. developed a volume-preserving (or incompressibility) penalty defined as the integral of the absolute logarithm of the Jacobian so that local deviations of the Jacobian from one can be penalized [18].

2.1.1 Rigidity

Rigidity penalties imposed on the subregions of the image volume which are anatomically rigid have been also developed for deformable image registrations [19-21]. A rigidity penalty term proposed by Loeckx *et al.* was based on the orthonormality of the deformation gradient tensor and was defined as the summation of the Frobenius norm of the orthonormality condition [19]. Staring *et al.* applied the orthonormality-preserving rigidity

penalty combined with the affinity penalty which requires the second order derivatives of the displacement to be zero and the properness penalty which requires the determinant of the deformation gradient tensor to be one [21]. For simplicity, this improved penalty will be referred to as the orthonormality-based rigidity penalty in this thesis. They tested the method on the images of three dimensional thorax CT and digital subtraction angiography. However, this orthonormality-based rigidity penalty has a potential to fail to properly work with images that contain multiple rigid bodies in close proximity such as cervical vertebrae in the neck region as considered in this investigation; in fact, the "existing" orthonormality penalties do not work properly with these images. Since the existing penalty lacks the ability to separately preserve rigidity of multiple objects in a close proximity, imposing the penalty on regions containing interfaces between rigid bodies (which exhibit abrupt change in displacement field) would result in displacement fields that are either unrealistically smooth, and thus fail to accurately capture the motions between rigid vertebral bodies.

2.1.2 Linear elasticity

Previous studies have incorporated linear elasticity into DIR in different ways; a systematic classification of DIR methods can be found in a recent review [22]. Many of the DIR methods, which adopted linear elasticity, were commonly based on the assumption that the resultant deformation maps should satisfy the static equilibrium for linear elastic materials represented as partial differential equations.

First, linear elasticity can be incorporated into DIR by directly solving the partial differential equations via an iterative process, such as the finite difference method, as suggested by Broit [23]. Once this initial concept was introduced, the method was refined with a multi-resolution strategy by Bajcsy and Kovacic [24]. In this approach, the gradient of image similarity metric was considered to be the body force in the partial differential equations.

On the other hand, linear elasticity can be introduced in a form of penalty in the optimization process of DIR. Christensen *et al.* used a linear elasticity penalty to support a consistent image registration [25]. In this previous study, the linear elasticity penalty was designed to constrain deformations to obey the laws of continuum mechanics. The authors investigated the impact of the linear elasticity penalty term on the accuracy of a DIR algorithm. By using the linear elasticity penalty, the accuracy was improved for the DIR of magnetic resonance and CT image data of human brain. However, this linear elasticity penalty (or any other physically-based penalty) has not been introduced to the DIR of soft tissue region in head and neck (HN) CT images.

2.2 Evaluation of Deformable Image Registration Accuracy

One of the qualitative evaluation methods for DIR is to compare the reference and the deformed target image by the resultant deformation map. However, a visual inspection of intensity-matching quality between the images does not always assure that the deformations are physically meaningful.

In addition, the quantitative measures, which have been frequently used in many previous investigations, may misinterpret the registration results. First, a volume overlap index has been frequently used in order to evaluate the registration accuracy [14, 26-27]. Although the volume overlap index is a good predictor of auto-contouring accuracy, a high score of the index is not necessarily related to accurate voxel-by-voxel deformation which is required for dose accumulation. Second, image similarity metrics such as normalized correlation coefficient, used in previous works [12, 15], may not be robust surrogates of the registration accuracy as reported in [10]. Finally, target registration error [12, 14-15, 26-32], which is defined as the difference between the distance of a landmark pairs and the displacement obtained by DIR, is one of the most popular measures. However, the target registration error was calculated with a limited number of landmarks, with which the accuracy of the volumetric deformation cannot be rigorously evaluated.

2.2.1 Finite element-based deformable image registration

Finite element (FE)-based DIR methods have been introduced in order to generate physically plausible deformation by utilizing anatomical information and mechanical properties. Finite element method is a numerical technique to find an approximate solution of the partial differential equations of static equilibrium. The solution of deformation analysis, for instance, is displacement vector fields (DVFs) calculated at the nodes of geometric elements, called finite elements, given displacement or force boundary conditions.

Various types of FE-based DIR algorithms have been developed [26-34]. In many of FE-based DIR algorithms, displacement boundary conditions for a few organs or anatomical regions are first obtained from the patient images and then those displacements are propagated to the entire region of interest. In Brock *et al.* [28], a FE model-based multi organ registration framework was developed by using a surface projection method in a commercial software package (HyperMorph) to obtain displacements at organ boundaries, and then was followed by a FE analysis to obtain deformation in internal structures. Al-Mayah *et al.* applied this FE-based DIR strategy to the problem of aligning of HN CT and CBCT images [26]. To the best of my knowledge, this technique proposed by the authors is the only FE-based method for the DIR of HN images. The boundary conditions were obtained by rigid alignments of bony components such as mandible and cervical vertebrae (C1−C7), and surface projection of exterior body. However, their method resulted in relatively large target registration errors in terms of average center volume error, which were reported as 2.3, 2.5, and 2.0 mm for tumor, left parotid, and right parotid, respectively; these large errors are partially due to the errors associated with the process of obtaining the boundary conditions, such as rigid registration for bony elements and surface projection for soft tissues.

2.2.2 Finite element-based accuracy evaluation

Development of FE-based accuracy evaluation framework has gathered strong interest in recent years because of its ability to generate realistic deformations through numerical simulation of patient motions, allowing voxel-by-voxel accuracy evaluation. In Schnabel *et al.* [35], a FE

method-based evaluation framework for DIR of breast magnetic resonance (MR) images was introduced. The basic idea of the framework is to compare the resultant DVFs obtained by DIR with the ground-truth DVFs generated by FE analysis. It is noteworthy to mention that DIR is performed on pairs of (1) synthetic reference image deformed by the corresponding ground-truth DVF and (2) original target image. In this previous study, physically plausible deformations were computed by applying boundary conditions assumed to be likely to occur *in vivo* to the FE models. The FE -based evaluation framework is generic so it can be extended to the accuracy evaluation of DIR of various regions.

However, for DIR of HN images, any FE-based evaluation framework has not been developed. The accuracy of the DIR of HN images has been evaluated by using a limited number of landmarks in the previous work. Although a recent study by Kirby *et al.* evaluated the accuracy of B-spline DIR by using a two-dimensional neck phantom having 54 surface markers, the phantom still needs to be refined with more anatomical details in order to thoroughly understand the behavior of DIR algorithms on head and neck images.

A special care needs to be taken when using finite element method to evaluate the accuracy of finite element-based deformable image registration algorithm. This is particularly relevant when the same boundary conditions are used both to generate the ground-truth DVFs and find DVFs to align images. In this experimental setting, the assumption that the deformation generated by finite element analysis is close to the deformation in vivo, needs to be carefully examined. If a FE model is too simple to generate realistic DVFs similar to those seen from patients, there is a possibility that the error of a FE-based DIR algorithm may be underestimated.

For instance, in Zhong *et al.* [34], the DVFs generated by a FE -based DIR algorithm were compared to the benchmark DVFs generated by simulating the same FE model. The registration error of 1.1 mm reported in this study, which is relatively small, need to be cautiously interpreted. Since the ground-truth DVFs were generated by using the same FE model, it might not be a challenging task for the FE-based DIR algorithm to cover the DVFs of same kind.

Chapter 3. Distance-Preserving Rigidity Penalty on Deformable Image Registration of Multiple Skeletal Components in the Neck

3.1 Overview

This study aims at developing and testing a novel penalty suitable for the deformable registration of tightly located skeletal components in the head and neck (HN) from planning computed tomography (CT) and daily cone-beam CT (CBCT) scans of patients undergoing radiotherapy. The proposed rigidity penalty is designed to preserve inter-voxel distances within each bony structure. This penalty was tested in the B-spline deformable image registration (DIR) of five cervical vertebral bodies (C1-C5). The displacement vector fields (DVFs) from the registrations were compared to the DVFs generated by using rigid body motions of the cervical vertebrae, measured by the surface registration of vertebrae delineated on planning and treatment CT images. Twenty five pairs of planning CT (reference) and treatment CTs (target) from 5 HN patients were aligned without and with the penalty. An existing penalty based on the orthonormality of the deformation gradient tensor was also tested and the effects of the penalties compared. The mean magnitude of the maximum registration error with the proposed distance-preserving penalty was (0.86, 1.12, 1.33) mm compared to (2.11, 2.49, 2.46) without penalty and (1.53, 1.64, 1.64) with the existing orthonormality-based penalty. The improvement in the accuracy of the DIR was also verified by comparing the Procrustes distance between the DVFs.

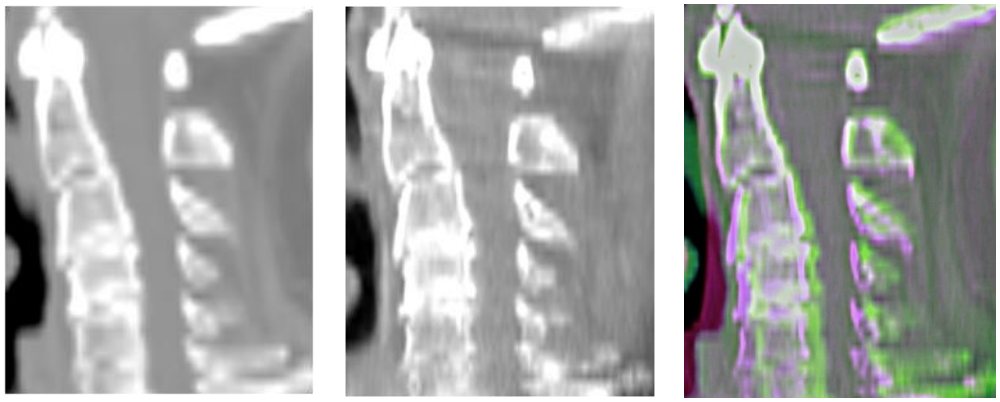

(a) (b) (c)

Fig. 3-1. Sagittal cuts of (a) a planning CT image and (b) a treatment CBCT image, and (c) the rigid alignment of the images at the C2 vertebra.

With the proposed penalty, the average distance was 0.11 (σ 0.03 mm) which is smaller than 0.53 (0.1 mm) without penalty and 0.28 (0.04 mm) with the orthonormality-based penalty. The accuracy of aligning multiple bony elements was improved by using the proposed distance-preserving rigidity penalty. The voxel-based statistical analysis of the registration error shows that the proposed penalty improved the integrity of the DVFs within the vertebral bodies.

3.2 Methods

A new rigidity penalty was developed in order to improve the accuracy of DIR of the cervical vertebrae in the neck, where the deformation occurs mainly due to neck articulation. Rigid alignment is clearly insufficient to describe daily variations, as illustrated in Fig. 3-1. Setup based on rigid alignment of the reference and target images at the C2 vertebra, while minimizing the likelihood of increased dose to the spinal cord for this particular treatment,

results in significant variations of the locations of the remaining vertebra and the neck as a whole.

3.2.1 Deformable image registration

DIR computes a voxel-to-voxel transformation $\varphi(\boldsymbol{x})$ of coordinates $\boldsymbol{x}$ of the reference image with intensity field I_R to the ones of the target image with intensity field I_T. Intensity-based DIR is, in general, formulated as an optimization problem to find the transformation that minimizes the intensity difference between the reference and target images. Mutual information (MI) is one of the most commonly used similarity metrics between images with different contrasts [36-37].

Typically, the displacement $\boldsymbol{u}$ of the target image from the reference image is approximated as linear combination of B-spline basis functions [38]

$$\varphi(\boldsymbol{x}_k;\boldsymbol{c}_k) = \boldsymbol{x}_k + \boldsymbol{u}(\boldsymbol{x}_k;\boldsymbol{c}_k) \tag{3.1}$$

where $\boldsymbol{x}_k$ are the coordinates of the k-th voxels in the reference image. The optimal B-spline coefficients $\boldsymbol{c} = (\boldsymbol{c}_1, \boldsymbol{c}_2, \ldots, \boldsymbol{c}_n)$ for each B-spline knot are iteratively determined as in Equation (3.2) through numerical optimization:

$$\boldsymbol{c}^* = \arg\min_{\boldsymbol{c}} F(\boldsymbol{c}) \tag{3.2}$$

where $F(\boldsymbol{c})$ is the image dissimilarity metric.

Alternatively, the objective function can be a weighted sum of the image dissimilarity metric $F(\boldsymbol{c})$ and penalty term $P_{rigidity}(\boldsymbol{c})$ as

$$\boldsymbol{c}^{*} = \arg\min_{\boldsymbol{c}} \left\{ F(\boldsymbol{c}) + w \cdot P_{rigidity}(\boldsymbol{c}) \right\} \tag{3.3}$$

where w represents a weight factor.

In this study, a DIR with multi-resolution B-spline transformation was implemented using Elastix, which is open source software for rigid and DIR of images (www.isi.uu.nl/Elastix) [39]. The DIR begins with low resolution image which is down-sampled by a factor of 4 in the left-right (LR) and anterior-posterior (AP) directions. Then, the resolution of the reference and target images are doubled after each levels of registration are finished.

3.2.2 Existing orthonormality-based rigidity penalty

The orthonormality condition of the deformation gradient tensor $\boldsymbol{F} = \partial\varphi(\boldsymbol{x})/\partial\boldsymbol{x}$ is equivalent to the condition of zero strain tensor or zero right Cauchy-Green tensor, according to the finite strain theory [40]. Typically, the orthonormality-preserving rigidity penalty term can be described as the sum of the squared Frobenius norm of $\boldsymbol{F}^{\mathrm{T}}\boldsymbol{F} - \boldsymbol{I}$ over the rigid regions in reference images [19]. Staring *et al.* improved this orthonormality-based rigidity penalty by

supplementing with two other conditions (affinity and properness, as previously mentioned) [21]. For simplicity, this improved penalty will be referred to as the orthonormality-based rigidity penalty in this manuscript.

3.2.3 Proposed distance-preserving rigidity penalty

The proposed rigidity penalty term is based on fundamental geometric characteristic of rigid bodies: the distance between any two points in a rigid body should remain constant after deformation. Similarly, the distance between any two voxels, which belong to the same rigid object, is required to be constant before and after deformation. By imposing this constraint only on voxel pairs within the same rigid object, the proposed rigidity penalty has the advantage that rigidities enforced to multiple rigid objects can be uncoupled. On the other hand, the existing rigidity penalties enforced to different rigid regions may become interrelated in a close proximity since their values are simply determined by local deformation gradients at a voxel, not depending on which rigid region the voxel and neighboring voxels belong to.

The penalty term is defined as the normalized sum of the squared difference of squared inter-voxel distance within each rigid body; for each voxel of a rigid component, the sum of the squared difference is normalized to the number of voxels that belong to both the same rigid object and its neighborhood, and the overall sum is normalized to the total number of voxels in rigid bodies:

$$P_{rigidity}(\boldsymbol{c}) = \frac{\sum_{i\in\{1,\ldots,N_R\}} \sum_{j\in R_i} \frac{1}{|R_i \cap P_j|} \sum_{k\in R_i\cap P_j} \left[\left\{ d'_{jk}(\boldsymbol{c}) \right\}^2 - d_{jk}^{\,2} \right]^2}{\sum_{i\in\{1,\ldots,N_R\}} |R_i|} \tag{3.4}$$

where N_R is the number of rigid bodies in the reference image, $R_i \subset \{1, 2,\ldots, N\}$ is a set of indices of voxels that belong to the i-th rigid body, $P_j \subset \{1, 2,\ldots, N\}$ is a set of indices of voxels that belong to the neighborhood of the j-th voxel (26-connected voxels are considered neighbors of a voxel), and

$$d_{jk} = \left\| \boldsymbol{x}_j - \boldsymbol{x}_k \right\| \tag{3.5}$$

$$d'_{jk}(\boldsymbol{c}) = \left\| \varphi(\boldsymbol{x}_j;\boldsymbol{c}_j) - \varphi(\boldsymbol{x}_k;\boldsymbol{c}_k) \right\| = \| \boldsymbol{x}_j + \boldsymbol{u}(\boldsymbol{x}_j;\boldsymbol{c}_j) - \boldsymbol{x}_k - \boldsymbol{u}(\boldsymbol{x}_k;\boldsymbol{c}_k) \|. \tag{3.6}$$

3.2.4 Case study

DIRs were performed on 25 pairs of the planning and treatment CT images from 5 patients and the corresponding ground-truth DVFs were generated by using the rigid transformations measured by surface registrations of the surface models of the cervical vertebrae.

Before performing DIRs, each pair of the planning CT and daily treatment CT images were roughly aligned by rigid registration. For the DIR, a multi-resolution strategy was utilized (three resolutions were applied in this study). After each level of registration, reference and target images were up-sampled by a factor of 2 only in the transverse plane so that the final

resolution reached the resolution of the original images. For the three resolutions, the B-spline grid spacing was set to 32, 16, and 8 voxels in the transverse plane; at the final level of the registration with the highest resolution, the B-spline grid spacing was set to 1 voxel through the axial direction. The voxel sizes of the planning CT images ranged from (0.94, 0.94, 3.0) mm to (1.37, 1.37, 3.0) mm.

For fair comparisons, the existing orthonormality-based penalty developed by Staring *et al.* and the proposed distance-preserving rigidity penalty were both implemented on Elastix, which is open source software for DIR. For both penalties, a gradient descent algorithm was utilized with 300, 300, and 500 iterations defined for the three resolutions [41]. The parameter *a*, which controls the gain factor in the optimization algorithm (see Spall *et al.*), was set to $a = 10000.0$ for all experiments except with large weight parameters; with $w = 0.2$ for the existing rigidity penalty and $w = 0.02$ for the proposed rigidity, the parameter was halved to 5000.0 for convergence.

3.2.4.1 Generation of the computed DVFs

In order to generate the ground-truth DVFs for each image pair, the planning CT image and 5 daily treatment CT images for each of 5 patients were subject to segmentation and surface model generation. Voxels that belong to the five cervical vertebrae were automatically segmented by thresholding intensity values on both the reference and target images, and manual modifications were applied for separating each vertebral body from neighboring ones. The segmented voxel sets were then converted to the corresponding surface models.

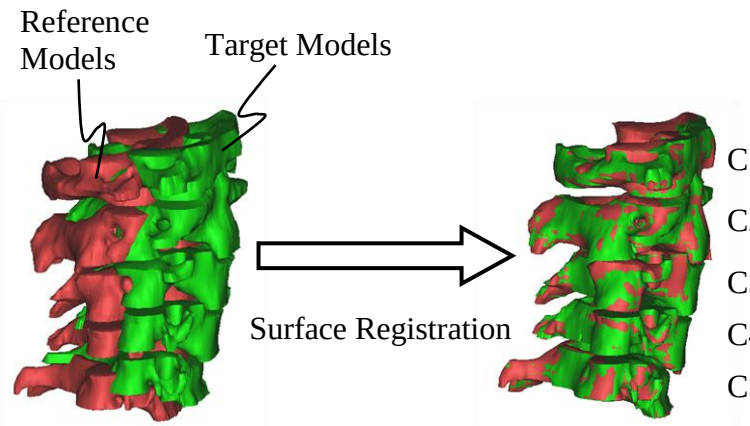

	Translation* (mm)	Rotation (°)
	LR − AP − IS	LR − AP − IS
C1:	-0.7, -2.8, 1.4	5.1, 0.7, -0.2
C2:	-0.4, -0.5, 1.9	7.5, 0.1, -1.6
C3:	-0.4, 2.1, 2.0	7.8, 0.8, -1.2
C4:	-0.7, 4.4, 2.2	6.1, 1.0, -0.5
C5:	-1.2, 6.5, 2.2	4.2, 1.8, 0.1

(a) (b) (c)

Fig. 3-2. Illustration of surface registration: reference and target models (a) before and (b) after registrations, and (c) an example of measured translations and rotations. *The shift from rigid registration in reference to the C2 vertebra was subtracted from the translation vectors.

Rigid motions of the cervical vertebrae were measured by registering the surface models by minimizing the distances between them. The registration of each pair of the surface models results in a 4 × 4 transformation matrix from which a translation vector and rotation angles are calculated. The initial alignment in reference to the C2 vertebra was subtracted from the resultant translation vector. An example pair of the surface models before and after the registrations is shown in Fig. 3-2 (a) and (b), respectively, and an example of the resulting translations and rotations are summarized in Fig. 3-2 (c) for the LR, AP, and inferior-superior (IS) axes, indicating that each bony element individually moved somewhat relative to the neighboring elements; the rotation centers were the average coordinates of voxels within each vertebra.

Finally, the ground-truth DVFs were calculated by using the rigid transformations, which were measured by the surface registrations.

3.2.4.2 Evaluation of registration accuracy

DIRs were performed on the 25 pairs of the planning CT images and the treatment CT images under three different conditions: (1) without rigidity penalty, (2) with the existing rigidity penalty, and (3) with the proposed rigidity penalty. Plotting the DVFs from registrations with the ground-truth DVFs allows qualitative evaluation of the registration accuracy. The registration accuracy was quantitatively evaluated by using three measures: registration error, transformation error, and the Procrustes distance. The registration error is defined as the difference between the ground-truth DVF (generated by using surface registration) and the DVF obtained by registration. The registration error was calculated at only the image voxels which belong to five cervical vertebral bodies. The transformation error was defined as the difference between the measured transformation of the vertebral body surfaces and the average transformation in DVF of points contained therein obtained by registration. The average transformation was obtained by solving the orthogonal Procrustes problem [42]: minimizing the distance between the original coordinates of each rigid body and its deformed coordinates. The transformation error was calculated for 6 degrees of freedom: 3 for translation and 3 for rotation. Translation was calculated as the distance between the geometric means of the original and deformed coordinates of voxels within vertebrae. The "Procrustes distance" was defined as the distance between the deformed coordinates from the DVF and the transformed coordinates by

the average transformation. This analysis evaluates the effect of the penalties on preserving the shape of the voxel grid in each bony element, by quantifying the residual local deformation using the translation vector and rotation matrix obtained by the orthogonal Procrustes analysis.

3.3 Results

The weight parameter *w* was experimentally determined in order to control the relative effect between the image metric and penalty term. Since the magnitude of the image discrepancy measure (negative of mutual information) is less than 1 and both the rigidity penalty terms are normalized to the number of voxels that belong to rigid regions, it can be expected that the magnitude of the weight parameter would not differ significantly from 1. The weight parameter was optimized by performing deformable image registrations with a few choices of weight parameters. The resulting optimal weights were 0.1 for the existing rigidity penalty and 0.01 for the proposed rigidity penalty. In addition, the relative weights of each terms related to affinity, orthonormality, and properness were chosen as 100.0, 1.0, and 2.0, respectively, in the existing orthonormality-based penalty, which were already optimally chosen for the alignment of CT images in Staring *et al*. [21]. It was also reported, in their study, that the registration results with the existing orthonormality-based rigidity penalty were not sensitive to the selection of the relative weights. All registrations with the proposed distance-preserving rigidity penalty were completed within 7 minutes on computers of a cluster which is comprised of AMD Opteron and Intel Nehalem processors.

Table 3-1 Translation in the LR, AP, and IS directions of the five cervical vertebrae compared to the planning CT image taken prior to the start of radiation treatment. Values are expressed as mean (SD) [Range].

	Left-Right (mm)	Anterior-Posterior (mm)	Inferior-Superior (mm)
C1	0.1 (0.7) [−1.6 to 1.5]	−0.6 (1.2) [−2.8 to 1.8]	−0.3 (0.8) [−2.2 to 1.4]
C2	0.0 (0.4) [−0.7 to 0.6]	−0.2 (0.4) [−0.9 to 0.8]	0.0 (0.8) [−1.5 to 1.9]
C3	0.1 (0.5) [−1.2 to 0.9]	0.4 (1.2) [−2.0 to 2.2]	0.3 (0.8) [−0.9 to 2.0]
C4	0.2 (1.1) [−2.1 to 2.3]	0.7 (2.2) [−3.5 to 4.4]	0.7 (0.9) [−0.9 to 2.2]
C5	0.1 (1.6) [−2.9 to 3.3]	0.9 (3.2) [−5.0 to 6.5]	0.8 (0.9) [−0.8 to 2.7]

Table 3-2 Rotations about the LR, AP, and IS axes of the five cervical vertebrae compared to the planning CT image taken prior to the start of radiation treatment. Values are expressed as mean (SD) [Range].

	Left-Right (°)	Anterior-Posterior (°)	Inferior-Superior (°)
C1	0.4 (2.1) [−3.3 to 5.1]	0.2 (1.0) [−1.9 to 1.9]	−0.4 (2.6) [−3.4 to 6.6]
C2	2.2 (3.2) [−3.0 to 7.5]	0.1 (1.2) [−2.8 to 2.6]	0.2 (2.6) [−4.0 to 5.8]
C3	2.1 (3.6) [−4.7 to 7.8]	0.2 (1.2) [−1.9 to 2.9]	0.0 (2.5) [−4.4 to 4.7]
C4	1.5 (3.3) [−5.0 to 6.1]	−0.1 (1.6) [−2.5 to 3.2]	−0.1 (2.6) [−5.2 to 4.3]
C5	0.2 (2.8) [−3.8 to 5.4]	0.7 (1.3) [−1.3 to 3.2]	0.4 (2.2) [−4.1 to 3.9]

3.3.1 Generation of the computed DVFs

Among the measured translations and rotations obtained by the surface registration, the translation in the AP direction and the rotation with respect to the LR axis were largest. The translation was largest for lower cervical vertebra in all directions (farthest from the setup point for the patients). However, there was no clear correlation between the translations and rotations.

The statistics of the measured translations and rotations are summarized in Tables 3-1 and 3-2 where mean, standard deviation and range of the motions were shown for three directions: LR, AP, and IS. The translation along the AP axis was most outstanding, being the smallest at the C2 vertebra (patient positioning point for treatment) and larger for lower cervical vertebra with a maximum displacement of 6.5 mm. The largest rotation (7.8 °) was observed at the C3 vertebra about the LR axis. Furthermore, the largest rotation with respect to the IS axis was 6.6 °, which was observed at the C1 vertebra.

The mean of the displacement magnitude was largest at the lowest vertebra (C5) for all patients, and ranged from 0.9 mm to 4.0 mm across the patients. The maximum displacement was 8.8 mm at the C5 vertebra for patient.

3.3.2 Evaluation of registration accuracy

Figure 3-3 shows comparisons of the DVFs from registrations (blue) with the ground-truth DVF (red). Figure 3-4 shows the comparison of the planning CT image and the deformed treatment CT images generated by applying the DVFs from the registration. The DVFs without and with rigidity penalty (either existing or proposed) transformed bone voxels in the target image visibly close to those in the reference image, indicating that all image registrations performed reasonably well in terms of intensity matching. However, the detailed examination of the DVFs in Fig. 3-3 reveals that the unpenalized intensity-based deformable image registration resulted in the deformation maps that lacked biomechanical consistency in the skeletal elements, where considerable local deformation was observed in the vertebral bodies. The discrepancies of

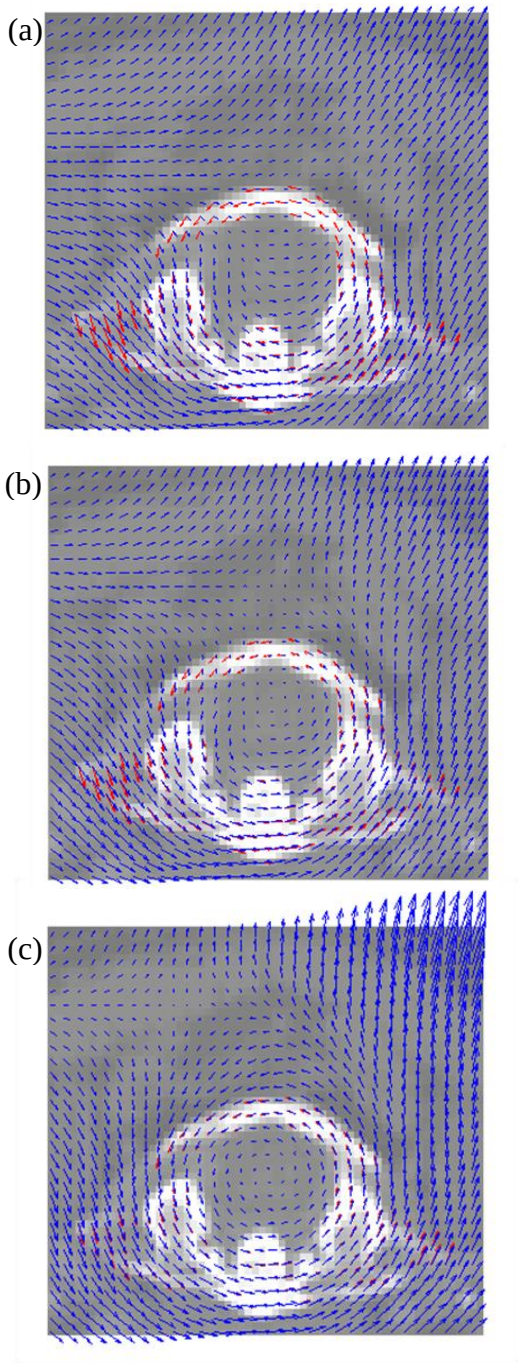

Fig. 3-3. Comparison of DVFs (blue) from registration (a) without penalty, (b) with the existing penalty, and (c) with the proposed penalty to the ground-truth DVF (red), which is plotted only at the bony regions.

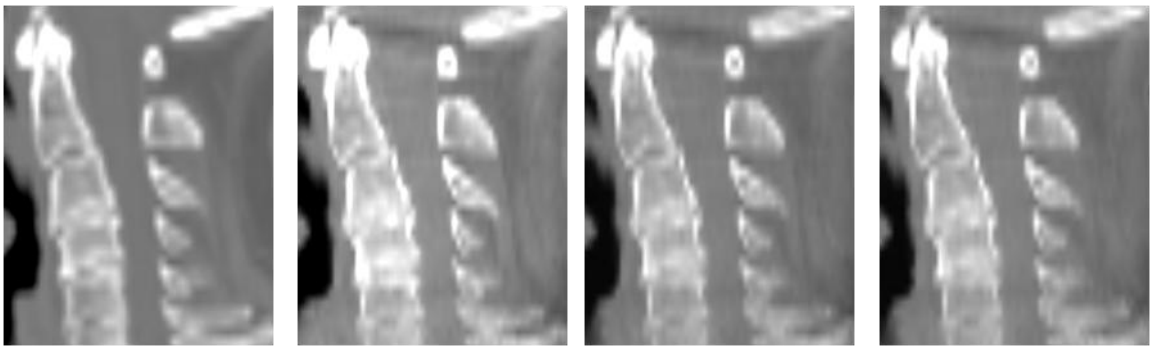

(a) (b) (c) (d)

Fig. 3-4. Sagittal cuts of (a) a planning CT image and treatment CBCT images deformed by DVFs from registration (b) without penalty, (c) with the existing penalty, and (d) with the proposed penalty, corresponding to the DVFs shown in Fig. 3-3.

the DVFs compared to the ground-truth DVF, which can be seen from Fig. 3-3 (a) and (b), are due to relatively large rotation of C1 vertebra about the IS axis (6.6° in Fig. 3-3). This type of misalignment was well corrected by the proposed rigidity penalty while it can be still observed in the DVF with the existing rigidity penalty.

The mean magnitudes and standard deviations of the registration errors are summarized in Table 3-3. Compared to the mean magnitude of (0.42, 0.32, 0.57) mm obtained by the intensity-based deformable image registration without rigidity penalty, the mean magnitude of registration error was reduced to (0.13, 0.16, 0.38) mm with the proposed distance-preserving penalty. Furthermore, the values were also smaller than (0.21, 0.20, 0.43) mm obtained with the existing orthonormality-based penalty. The mean magnitude of the maximum registration error was also reduced by the proposed distance-preserving rigidity penalty to (0.86, 1.12, 1.33) mm

Table 3-3 Registration errors between the DVFs in the LR, AP, and IS directions of the five cervical vertebrae without and with the rigidity penalties.

		Intensity-based	Orthonormality-based	Distance-preserving
Registration Error (mm)	Mean magnitude	(0.42, 0.32, 0.57)	(0.21, 0.20, 0.43)	(0.13, 0.16, 0.38)
	Standard deviation	(0.38, 0.42, 0.61)	(0.23, 0.25, 0.34)	(0.11, 0.17, 0.26)
	Mean magnitude of maximum error	(2.11, 2.49, 2.46)	(1.53, 1.64, 1.64)	(0.86, 1.12, 1.33)

Table 3-4 Comparison of the transformation errors and Procrustes distance between the DVFs without penalty and with the rigidity penalties.

		Intensity-based	Orthonormality-based	Distance-preserving
Translation (mm)				
	Mean magnitude	(0.34, 0.13, 0.38)	(0.14, 0.11, 0.37)	(0.11, 0.11, 0.36)
	Standard deviation	(0.41, 0.16, 0.32)	(0.16, 0.13, 0.25)	(0.13, 0.13, 0.25)
Rotation (°)				
	Mean magnitude	(1.22, 0.50, 0.61)	(0.65, 0.32, 0.33)	(0.58, 0.34, 0.28)
	Standard deviation	(1.32, 0.62, 0.84)	(0.69, 0.40, 0.42)	(0.70, 0.45, 0.35)
Procrustes distance (mm)		0.53 (0.11)	0.28 (0.04)	0.11 (0.03)

as compared to (2.11, 2.49, 2.46) mm without penalty and (1.53, 1.64, 1.64) mm with the existing orthonormality-based rigidity penalty.

The mean magnitudes and standard deviations of the transformation errors are summarized in Table 3-4. For both the translations and rotations of all vertebrae, the errors were reduced by the rigidity penalties. The transformation errors resulting from the deformable image

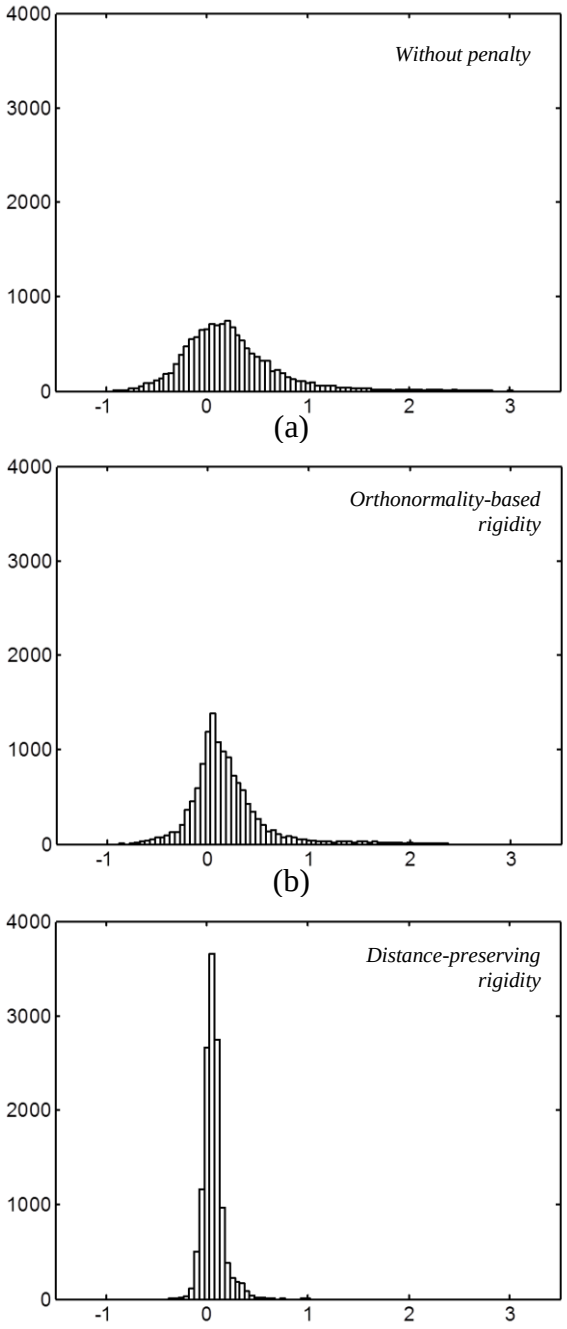

Fig. 3-5. Histograms of the registration errors which resulted from the B-spline DIRs between the planning CT scan and treatment CT scan at the 7th fraction of Patient 1 in the LR direction (a) without penalty, (b) with the existing orthonormality-based rigidity penalty, and (c) with the proposed distance-preserving rigidity penalty.

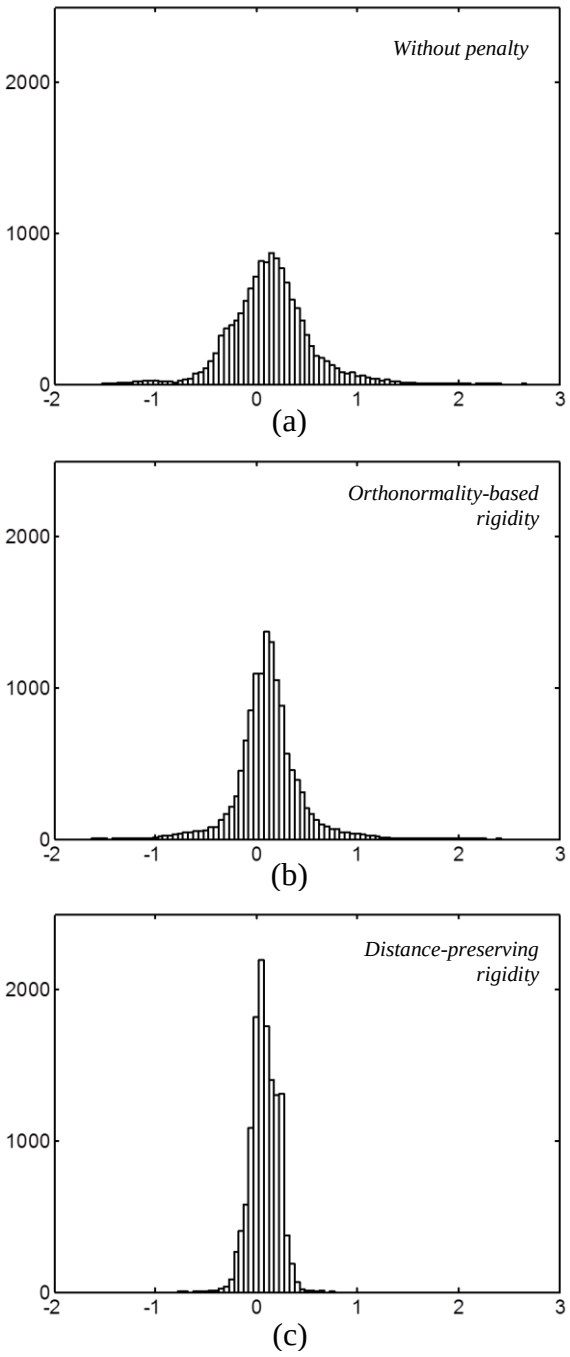

Fig. 3-6. Histograms of the registration errors which resulted from the B-spline DIRs between the planning CT scan and treatment CT scan at the 7th fraction of Patient 1 in the AP direction (a) without penalty, (b) with the existing orthonormality-based rigidity penalty, and (c) with the proposed distance-preserving rigidity penalty.

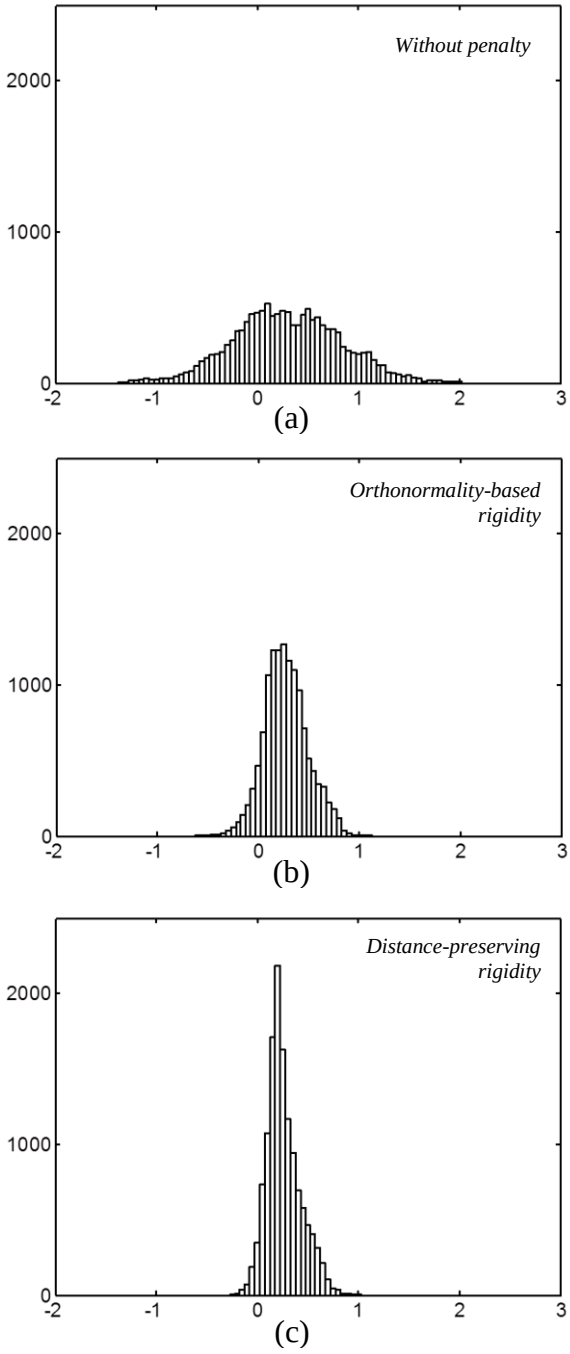

Fig. 3-7. Histograms of the registration errors which resulted from the B-spline DIRs between the planning CT scan and treatment CT scan at the 7th fraction of Patient 1 in the IS direction (a) without penalty, (b) with the existing orthonormality-based rigidity penalty, and (c) with the proposed distance-preserving rigidity penalty.

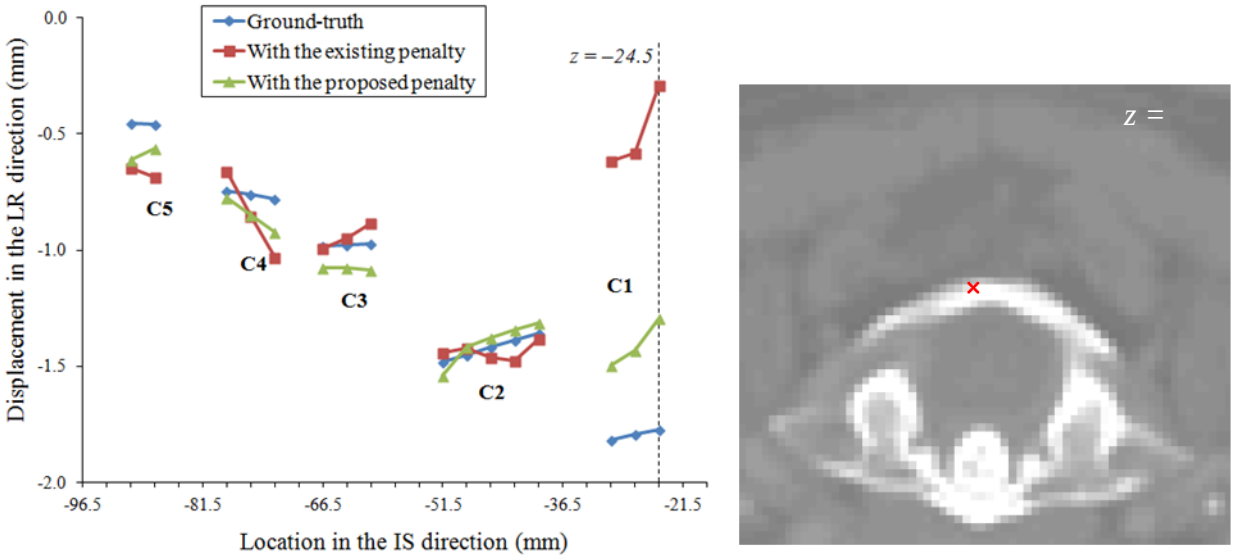

(a)(c) (b)

Fig. 3-8. Plots of (a) the LR displacement component through an IS axis whose location is indicated in (b) an axial cut of the planning CT (Patient 1); the axial plane in (b), which is indicated as a dashed line in (a), coincides with the axial plane in Fig. 3-3.

registration with the rigidity penalty terms were similar to each other. The Procrustes distances are also summarized in Table 3-4. The Procrustes distances for the proposed distance-preserving penalty were less than those for no rigidity penalty and the existing orthonormality-based penalty: 0.11 mm (0.03 mm) versus 0.53 (0.11 mm) and 0.28 mm (0.04 mm).

The difference of the effects of the penalty terms was further explored by plotting histograms of registration errors (Figures 3-5, 3-6, and 3-7). For the B-spline DIR without penalty, the registration errors were distributed over a wide range in all directions while many of the errors were still close to zero. With the distance-preserving rigidity penalty, the distribution of registration errors was better concentrated around zero than those without penalty or with the

existing orthonormality-based rigidity penalty, indicating that some large deviations were corrected by the proposed penalty.

The displacement components in the LR directions plotted in Fig. 3-8 (a) show how the resultant DVFs with the existing and proposed penalties recovered the ground-truth DVF exhibiting abrupt changes across the vertebrae. Compared to the DVF obtained with the existing orthonormality-based penalty, the DVF obtained with the proposed distance-preserving penalty more accurately recovered the acute changes in the displacement, especially at regions within the C1 vertebra.

In order to investigate the impact of the weight parameter on the registration accuracy with the rigidity penalties, DIRs were additionally performed by varying the weight parameters. The weight parameter was increased or decreased by a factor of 2 from the optimal weight parameter, which is 0.1 for the existing orthonormality-based rigidity penalty and 0.01 for the proposed distance-preserving rigidity penalty. The resultant registration errors were summarized in Tables 3-5 and 3-6. As the weight parameter was decreased from 0.01 to 0.0025 for the proposed distance-preserving rigidity penalty (from 0.1 to 0.025 for the existing orthonormality-based rigidity penalty), the registration errors were increased in all directions. Comparing the variations in the registration errors between the two rigidity penalties shows that the performance of the proposed distance-preserving rigidity penalty is less sensitive to the variation of the weight parameter than that of the existing orthonormality-based rigidity penalty.

Table 3-5 Effect of the weight parameter on the registration errors with the existing orthonormality-based rigidity penalty.

		$w = 0.025$	$w = 0.05$	$w = 0.1$	$w = 0.2$
Registration Error (mm)	Mean magnitude	(0.26, 0.25, 0.47)	(0.23, 0.22, 0.44)	(0.21, 0.20, 0.43)	(0.31, 0.22, 0.42)
	Standard deviation	(0.30, 0.32, 0.41)	(0.26, 0.28, 0.37)	(0.23, 0.25, 0.34)	(0.25, 0.28, 0.34)
	Mean magnitude of maximum error	(1.77, 2.15, 1.94)	(1.66, 1.91, 1.79)	(1.53, 1.64, 1.64)	(1.63, 1.56, 1.58)

Table 3-6 Effect of the weight parameter on the registration errors with the proposed distance-preserving rigidity penalty.

		$w = 0.0025$	$w = 0.005$	$w = 0.01$	$w = 0.02$
Registration Error (mm)	Mean magnitude	(0.14, 0.16, 0.40)	(0.13, 0.16, 0.39)	(0.13, 0.16, 0.38)	(0.31, 0.19, 0.38)
	Standard deviation	(0.13, 0.18, 0.29)	(0.12, 0.17, 0.28)	(0.11, 0.17, 0.26)	(0.16, 0.22, 0.27)
	Mean magnitude of maximum error	(1.02, 1.38, 1.55)	(0.94, 1.26, 1.44)	(0.86, 1.12, 1.33)	(1.17, 1.04, 1.16)

For the large weight parameters ($w = 0.2$ for the existing orthonormality-based rigidity penalty and $w = 0.02$ for the proposed distance-preserving rigidity penalty), the registration results shown in Tables 3-5 and 3-6 were obtained with $a = 5000$. This is because the registrations converged to unreasonable solutions when the gain factor a was set to 10000, possibly indicating a numerical instability of the optimization algorithm.

3.4 Discussion

The proposed distance-preserving rigidity penalty improved the accuracy of deformable image registration of the five cervical vertebral bodies in the neck compared to B-spline intensity-based deformable image registration without the rigidity penalty. All quantification measures utilized in this study showed the proposed distance-preserving rigidity penalty better aligned the five cervical vertebrae in CT-CBCT registrations than the existing orthonormality-based rigidity penalty. It is noteworthy to mention that, with the proposed penalty, the B-spline DIR of the cervical vertebrae achieved accuracies smaller than the sizes of image voxels in all directions. The mean magnitudes and standard deviations of the registration errors were (0.13, 0.16, 0.38) mm and (0.11, 0.17, 0.26) mm. Furthermore, the mean magnitudes of the maximum registration errors were comparable to the voxel dimensions: (0.86, 1.12, 1.33) mm with the proposed distance-preserving penalty. It is noted that the registration accuracy was largest in the IS direction, in which the voxel dimension is larger than that in the LR and AP directions. However, the achieved registration accuracy was much smaller than the voxel dimension.

Since the registration errors were averaged over a large number of voxels (12,986–22,653) that belong to the cervical vertebrae, some improvements may not appear in the comparisons of the mean magnitudes of the registration errors. In other words, the statistics of the registration errors calculated at a large number of the voxels may not be considered as an equivalent concept to the target registration error calculated with a few number of landmark pairs as shown in other studies [10, 12]. As shown in the histograms of the registration errors (Figures 3-5, 3-6, and 3-7), purely intensity-based DIR failed to recover all rigid body motions of the five

cervical vertebrae. Moreover, the discrepancies observed in the C1 vertebra were not corrected by the existing orthonormality-based rigidity penalty while these registration errors were prevented by applying the proposed distance-preserving rigidity penalty to deformable image registration.

The comparisons of the transformation errors and Procrustes distances between the DVFs showed the details of how the proposed penalty improved the DVFs compared to no penalty and the existing penalty. The difference in the Procrustes distance between the DVFs was relatively large while the transformation errors were comparable to each other. The relatively small difference in transformation error indicated that the DVFs with the existing penalty were, on average, shaped closely to the ground-truth rigid motions. However, the large values in the Procrustes distance for the DVFs with the existing penalty indicated that there exist some discrepancies in the resulting DVFs compared to the ground-truth DVFs, which cannot be captured by the transformation errors. These results suggest the proposed distance-preserving penalty is capable of reducing registration errors, which cannot be completely corrected by the existing orthonormality-based penalty in the DIR of multiple rigid bodies in close proximity.

The comparison of the DVFs indicated that the intensity-based similarity metric may potentially mislead deformable image registration in articulated skeletal regions. As shown in Fig. 3-3, the B-spline DIR of the HN images resulted in physically unreasonable DVFs without rigidity penalties. However, these substantial deviations in the DVF were not visible in the comparison of images in Fig. 3-4. This observation supports that comparing images is not a rigorous way of verifying registration results as well as that intensity-driven DIR should be

provided with additional guidance such as biomechanical penalties when the transformations are to be used for dose accumulation or functional mapping.

The use of the rigidity penalty term may have an impact on the accuracy of dose accumulation of surrounding tissues such as spinal cord. As can be seen in Fig. 3-3, both the orthonormality-based and distance-preserving rigidity penalties affected the deformation in the surrounding regions. A further investigation needs to be carried out to estimate the dosimetric impact of such residual uncertainty.

Mutual information was used as an intensity similarity measure between planning CT and treatment CBCT images whose intensity distributions are different to each other although these images look similar. In a recent study by Nithiananthan *et al.* [12], mutual information was also used for B-spline DIR of CT and CBCT images. Since CT and CBCT images have different intensity distributions, an intensity matching approach was proposed for their implementation of a demons algorithm in the previous study. It is worthwhile to note that other intensity similarity measure such as normalized cross-correlation can be utilized for the CT to CBCT DIR. The impact of using various image similarity measures should be investigated in a future study.

The rigid motions measured by the surface registration of individual vertebrae ranged from −5.0 to 6.5 mm for translation and from −4.7 to 7.8 ° for rotation as shown in Tables 3-1 and 3-2. The results were comparable to those reported in Ahn *et al*. [43]. For the magnitude of relative vertebral motions clinically observed from the five patients, the proposed penalty could successfully preserve rigidity of five cervical vertebral bodies during deformable alignment.

3.5 Conclusions

We proposed a new rigidity penalty designed to preserve inter-voxel distance within each bony element and verified that it improved the integrity of the B-spline DIR of multiple skeletal components in the neck anatomy using 25 CT-CBCT image pairs from 5 patients. This distance-preserving penalty achieved sub-voxel registration accuracy in all directions and outperformed the existing penalty designed to preserve the orthonormality of deformable gradient tensor, in terms of aligning multiple rigid elements in close proximity.

Chapter 4. Elasticity Penalty for Deformable Image Registration of Muscle in the Neck

4.1 Overview

The objective of this study is to incorporate a penalty into the B-spline deformable image registration (DIR) of a neck muscle in head and neck (HN) patient images. The penalty was designed to prevent the resultant deformations from violating the static equilibrium equations for linear elastic materials. Homogeneous material properties were assumed on the sternomastoid muscle and the active behavior of the muscle was not taken into consideration. To investigate the impact of the penalty, B-spline DIRs were performed without and with the penalty between HN computed tomography (CT) and cone-beam CT (CBCT) images. In addition, the B-spline DIR was tested under various selections of the registration parameters associated with the image metric (mutual information) and the optimization algorithm (a gradient descent algorithm). The penalty helped the B-spline DIR to avoid large misalignments obtained without the penalty. This finding indicates that time-consuming fine-tuning process for the B-spline DIR to find a reasonable deformation map can be avoided by using the penalty.

4.2 Methods

4.2.1 Deformable image registration

The mathematical formulation of the B-spline DIR is shown in Chapter 3. For the B-spline DIR of a muscle in the neck, a penalty which preserves linear elasticity (called elasticity penalty $P_{elasticity}$) is used instead of the rigidity penalty $P_{rigidity}$ (see Equation (3.3)). Therefore, the formulation of the B-spline DIR can be written as follows:

$$\boldsymbol{c}^{*} = \arg\min_{\boldsymbol{c}} \left\{ F(\boldsymbol{c}) + w \cdot P_{elasticity}(\boldsymbol{c}) \right\}. \tag{4.1}$$

An optimal set of B-spline coefficients is obtained through an optimization problem that minimizes the cost function, which consists of an image dissimilarity measure and the elasticity penalty.

In this study, mutual information [36-37] was utilized as an image similarity measure. A multi-resolution strategy was adopted for the B-spline DIR between HN CT and CBCT images. In a multi-resolution B-spline DIR, the B-spline transformation is up-sampled by a factor of two after each level of resolution as the reference and target images are also up-sampled by a factor of two in all directions. The B-spline DIR was implemented using Insight Segmentation and Registration Toolkit (ITK) [44], which is an open-source software package for registration

algorithms. A gradient descent optimization algorithm, which is available in ITK, was chosen to update the B-spline coefficients through a series of iterations.

4.2.2 Elasticity penalty

A penalty term was designed to preserve linear elastic behaviors in the deformation by deformable image registration. In other words, the penalty term encourages the registration algorithm to satisfy the static equilibrium equations [45] as described in Equation (4.2):

$$\frac{\partial \sigma_{ij}}{\partial x_j} + f_i = 0 \tag{4.2}$$

where σ, x, and f represents stress tensor, coordinates, and body force, respectively. It is noted that Equations (4.2) – (4.7) are described in tensor notation. These differential equations can be written in terms of displacement vector u by substituting for the stress tensor with the stress-strain relationship (Equation (4.3)) and strain-displacement relationship (Equation (4.4)):

$$\sigma_{ij} = \frac{E}{1+\nu}\varepsilon_{ij} + \frac{\nu E}{(1+\nu)(1-2\nu)}\delta_{ij}\varepsilon_{kk}, \tag{4.3}$$

$$\varepsilon_{ij} = \frac{1}{2}(u_{j,i} + u_{i,j}), \tag{4.4}$$

where E is Young's modulus and ν is Poisson's ratio. Finally, the static equilibrium equations become

$$\frac{E}{2(1+\nu)}u_{i,jj} + \frac{E}{(1+\nu)(1+2\nu)}u_{j,ij} + f_i = 0. \tag{4.5}$$

The body force in Eq. (4.5) was assumed to be zero at the convergence of optimization algorithm in the B-spline DIR. It is contrasted with the case of numerically solving the equations where the gradient derived from an image similarity metric was considered as the body force [23]. The elasticity penalty $P_{elasticity}$ can be defined as in Equation (4.6) in order to prevent the displacement vector field from violating the static equilibrium equations.

$$P_{elasticity}(\boldsymbol{c}) = \frac{\sum_{m\in S}\left\| \frac{E}{2(1+\nu)}u_{i,jj}(\boldsymbol{c}) + \frac{E}{(1+\nu)(1+2\nu)}u_{j,ij}(\boldsymbol{c}) \right\|_m^2}{|S|} \tag{4.6}$$

where the displacement vector field is represented by the B-spline coefficients $\boldsymbol{c}$. The penalty is calculated by summing up the deviations from the equations at each mth point in a set of voxels belonging to the region of interest S and by normalizing the sum to the number of the voxels.

The equation above can be further simplified by dividing the whole equation by $E/2(1+\nu)$ as follows:

$$P_{elasticity}(\boldsymbol{c}) = \frac{\sum_{i \in S} \left\| u_{i,jj}(\boldsymbol{c}) + \frac{2}{1+2\nu} u_{j,ij}(\boldsymbol{c}) \right\|_i^2}{|S|}. \quad (4.7)$$

Young's modulus shown in Equation (4.6) is eliminated because it has the same impact on the B-spline DIR with the weight parameter *w* when the deformation in only a single muscle is penalized. When considering multiple regions with different material properties, different weight parameters may need to be set according to each region. For the implementation of the elasticity penalty, the second-order derivatives of the displacement vector field were calculated by using a finite difference method.

4.2.3 Case study

The B-spline DIRs (without and with the elasticity penalty) were performed on 7 data sets, in total, from 2 patients. The deformation maps were obtained by the B-spline DIRs from the HN planning CT images (reference images) to the treatment CBCT images of the same patient (target images). A data set of the reference and target images was shown in Fig. 4-1. (a) and (b). Each of the reference images was cropped to contain the sternocleidomastoid muscle on the side, on which no tumor exists. The image voxel dimensions ranged from 1.26 to 1.37 mm in axial planes and the slice thickness was 3.0 mm through the inferior-superior (IS) direction. The image voxels, which belong to the sternocleidomastoid muscle, were segmented by using the

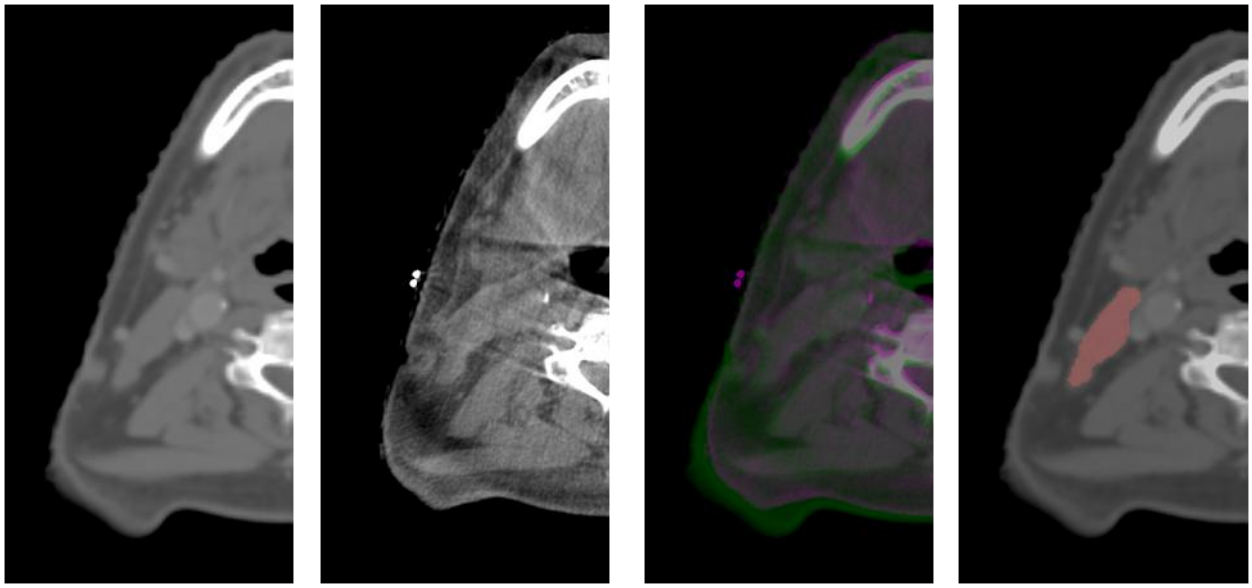

(a) (b) (c) (d)

Fig. 4-1. Axial cuts of (a) the planning CT, (b) the treatment CBCT of a head and neck cancer patient, (c) an overlaid volume of the images in (a) and (b), and (d) the planning CT with segmentation of sternocleidomastoid muscle.

intensity values of the voxels. Segmentation was performed both on the planning CT and treatment CBCT images. An axial cut of the segmentation performed on the reference CT image was shown in Fig. 4-1. (d).

4.2.3.1 Registration parameters

The parameters selected for the B-spline DIR were summarized in Table 4-1. Both the reference/target images and the B-spline transformation were up-sampled by a factor of 2 after each resolution level. While the full-resolution images were used at the final level, the B-spline

Table 4-1 Summary of the registration parameters selected for the B-spline deformable image registration of head and neck CT/CBCT image pairs. LR, AP, and IS stands for the left-right, anterior-posterior, and inferior-superior directions, respectively.

Registration parameters	Values used
Image resolutions	
Number of resolution levels	4
Up-sampling factor	2
Cubic B-spline transformation	
Grid spacing at final level (times voxel dimensions)	8 (LR, AP), 4 (IS)
Up-sampling factor	2
Mutual information (image metric)	
Percentage of image voxels used for the calculation (%)	10, 20, 30
Number of histogram bins	50
Regular step gradient descent optimization	
Gradient magnitude tolerance – at the coarsest level	0.002, 0.004
Gradient magnitude tolerance – factor	0.75 ,1
Step size – at the coarsest level	4, 16, 64
Step size – factor	0.25, 0.5, 1

grid spacing was set to be (8, 8, 4) times the image voxel dimensions of the reference image in the left-right (LR), the anterior-posterior (AP), and IS directions, respectively. The B-spline DIR was performed with various parameters associated with the image similarity metric and optimization algorithm. To calculate the mutual information between the two images matched

by the B-spline DIR, different fractions of the voxels within the entire region of reference image were utilized: 10, 20, and 30 %. For the gradient descent optimization algorithm, different values were used for the convergence criterion, which is defined by the gradient magnitude of the cost function, and the step size, with which the B-spline coefficients (design variables) are updated along the direction of the gradients. For both the gradient magnitude tolerance and the step size, two parameters are chosen, that is, its value at the coarsest level and the factor by which it is multiplied as summarized in Table 4-1.

4.2.3.2 Evaluation of registration accuracy

Dice similarity coefficient (DSC) [46] was used in order to assess the accuracy of the B-spline DIR. DSC, defined as in Equation (4.8), is considered as a well-established measure for the registration accuracy at boundaries, i.e. auto-contouring accuracy.

$$s = \frac{2|A \cap B|}{|A| + |B|} \tag{4.8}$$

where A and B describe two different sets of voxels. If the two different sets coincide perfectly, the measure should be 1. On the other hand, the DSC value is zero at no overlap between the two sets of voxels.

For the accuracy evaluation of the B-spline DIR of the muscle, Equation (4.8) becomes

$$s(\boldsymbol{c}) = \frac{2\left|L_R \bigcap L_T(\boldsymbol{c})\right|}{\left|L_R\right| + \left|L_T(\boldsymbol{c})\right|} \tag{4.9}$$

where L_R represents a set of voxels labeled for the muscle region in reference image. The corresponding set of muscle voxels in target image is warped by the resultant B-spline transformation into the coordinates of the reference image, resulting in deformed target label L_T, which naturally becomes a function of the B-spline coefficients $\boldsymbol{c}$.

4.3 Results

The maximum DSCs were found as 88.9 % and 88.5 % for the B-spline DIRs without and with the penalty at the same image data sets, but with different registration parameters (see Table 4-2). The percentage of image voxels used for the calculation of the mutual information was 20 % for both methods. The tolerance for the gradient magnitude at the coarsest resolution level was 0.002 (with a factor of 0.75) vs. 0.004 (with a factor of 1). The step size at the coarsest level was 64 vs. 16 with this step size unchanged through the four resolution levels for both the B-spline DIRs. Figure 4-2 ((a) and (b)) shows the target labels of the muscle deformed by the deformation maps which are corresponding to the maximum DSCs. As can be seen in Fig. 4-2 (a) and (b), the deformed target labels fairly well aligned the sternocleidomastoid muscle seen in the planning CT image.

Table 4-2 Summary of the parametric settings with the maximum DSCs found for B-spline DIR of one of the image data sets.

Registration parameters	Without penalty	With penalty
Mutual information (image metric)		
Percentage of image voxels (%)	20	20
Regular step gradient descent optimization		
Gradient magnitude tolerance – at the coarsest level	0.002	0.004
Gradient magnitude tolerance – factor	0.75	1
Step size – at the coarsest level	64	16
Step size –factor	1	1
Maximum DSC value (%)	88.9	88.5

Table 4-3 Summary of the parametric settings under which the B-spline DIR resulted in highest DSCs values on average across the image data sets.

Registration parameters	Without penalty	With Penalty
Mutual information (image metric)		
Percentage of image voxels (%)	30	20
Regular step gradient descent optimization		
Gradient magnitude tolerance – at the coarsest level	0.002	0.002
Gradient magnitude tolerance – factor	0.75	0.75
Step size – at the coarsest level	64	16
Step size – factor	1	0.5
Maximum DSC value (%)	84.2 ± 3.2	84.2 ± 2.4

The parameters with which the B-spline DIR showed highest DSCs across the image data sets are shown in Table 4-3. The maximum DSC was 84.2 ± 3.2 (%) vs. 84.2 ± 2.4 (%), showing that the elasticity penalty has almost no impact on the maximum DSC by the B-spline DIR.

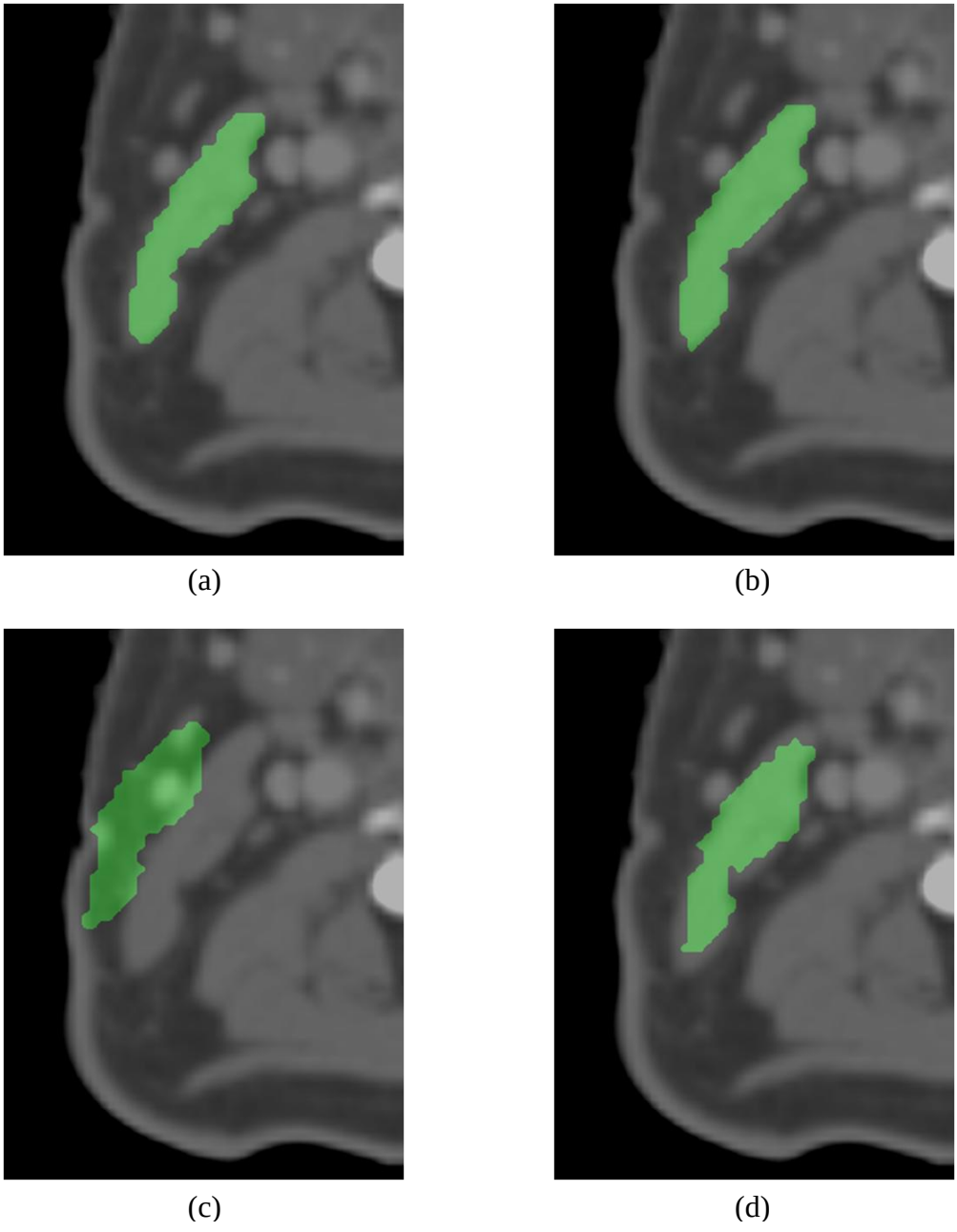

Fig. 4-2. Axial cuts of a planning CT image on which the deformed target labels of the muscle are overlaid. The muscle labels were deformed by the B-spline DIR (a), (c) without the penalty, and (b), (d) with the penalty. The corresponding DSC values are (a) 88.9 %, (b) 88.5 %, (c) 16.7 %, and (d) 77.8 %.

Comparing the DSC values obtained under various combinations of the parameters shows that the elasticity penalty improves the accuracy of the B-spline DIR. The DSC values, each averaged across the data sets were graphed in box plots (Fig. 4-3). The comparisons of the box plots show slight improvements in the DSC values by using the penalty: almost no increase in median (horizontal line in box plot), slight improvement in 1st and 3rd quartiles (bottom and top edges of box plot). With 8 parametric settings out of 108 tested, which are all associated with the step size of 64 at the coarsest level, increases in DSC larger than 10 % were achieved by using the elasticity penalty while the maximum decrease was 2.2 %.

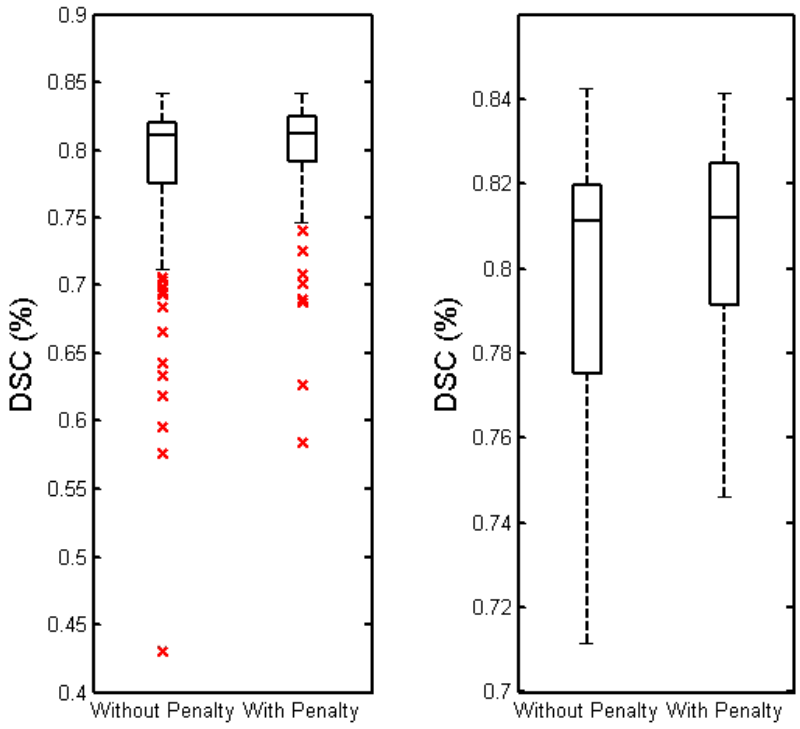

(a) (b)

Fig. 4-3. Box plots of the DSC values obtained with various parametric settings (each averaged across the data sets), showing a comparison between the cases without and with the penalty; a part of the box plots in (a) was enlarged in (b) for the detailed comparison of the box plots.

In order to see the improvements by using the elasticity penalty in detail, the DSC values obtained for one of the image data sets were graphed in box plots (Fig. 4-4). It is noted that the image data sets were chosen because the corresponding results showed the similar trends with those averaged across all image data sets, shown in Fig. 4-3. As an example of a relatively large improvement that can be achieved by using the elasticity penalty, the DSC value was increased from 16.7 % to 77.8 %. This improvement is also shown in Fig. 4-2 (c) and (d) by overlaying the deformed target labels on the planning CT image. This finding indicated that the elasticity penalty enabled the B-spline DIR to avoid large misalignments.

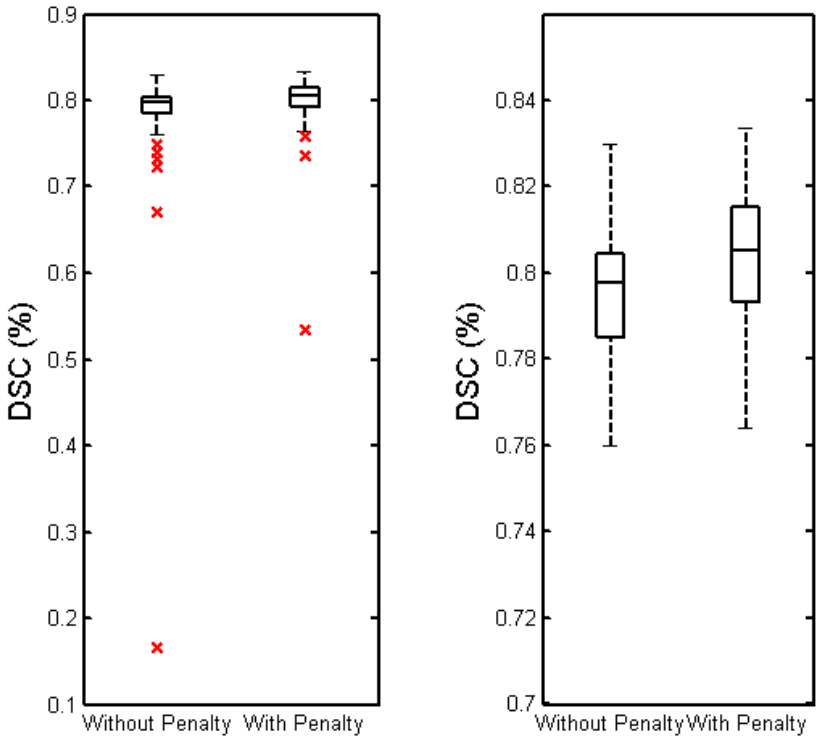

Fig. 4-4. Box plots of the DSC values obtained with various parametric settings (for one image data set); a part of the box plots in (a) was enlarged in (b) for the detailed comparison.

Table 4-4 Comparisons of mDSC and sDSC calculated from the resultant deformation maps by the B-spline DIR without vs. with the elasticity penalty (mean ± standard deviation, *p*-value obtained with a paired *t*-test).

	Without Penalty	With Penalty	*p*-value
mDSC (%)	78.4 ± 4.8	80.0 ± 3.5	0.04
sDSC (%)	8.3 ± 8.1	6.1 ± 5.5	0.14

For each data set, mean (mDSC) and standard deviations (sDSC) were calculated from the DSC values obtained under the different parametric settings. The mean and standard deviation from the data of mDSC, sDSC, maxDSC, and minDSC calculated for the 7 image data sets were presented in Table 4-4. By using the penalty, on average, mDSC was increased by 1.6 % and sDSC was reduced by 1.8 %. To test the statistical significance of the difference between the results obtained without and with the elasticity penalty, a paired *t*-test was performed. As results of the statistical test, it was found that the accuracy (mDSC) was improved across the registration parameters with a statistical significance ($p < 0.05$). To see the normality of the data, which is required for the *t*-test, Q-Q plots were generated for mDSC, sDSC, maxDSC, and minDSC as shown in Fig. 4-4.

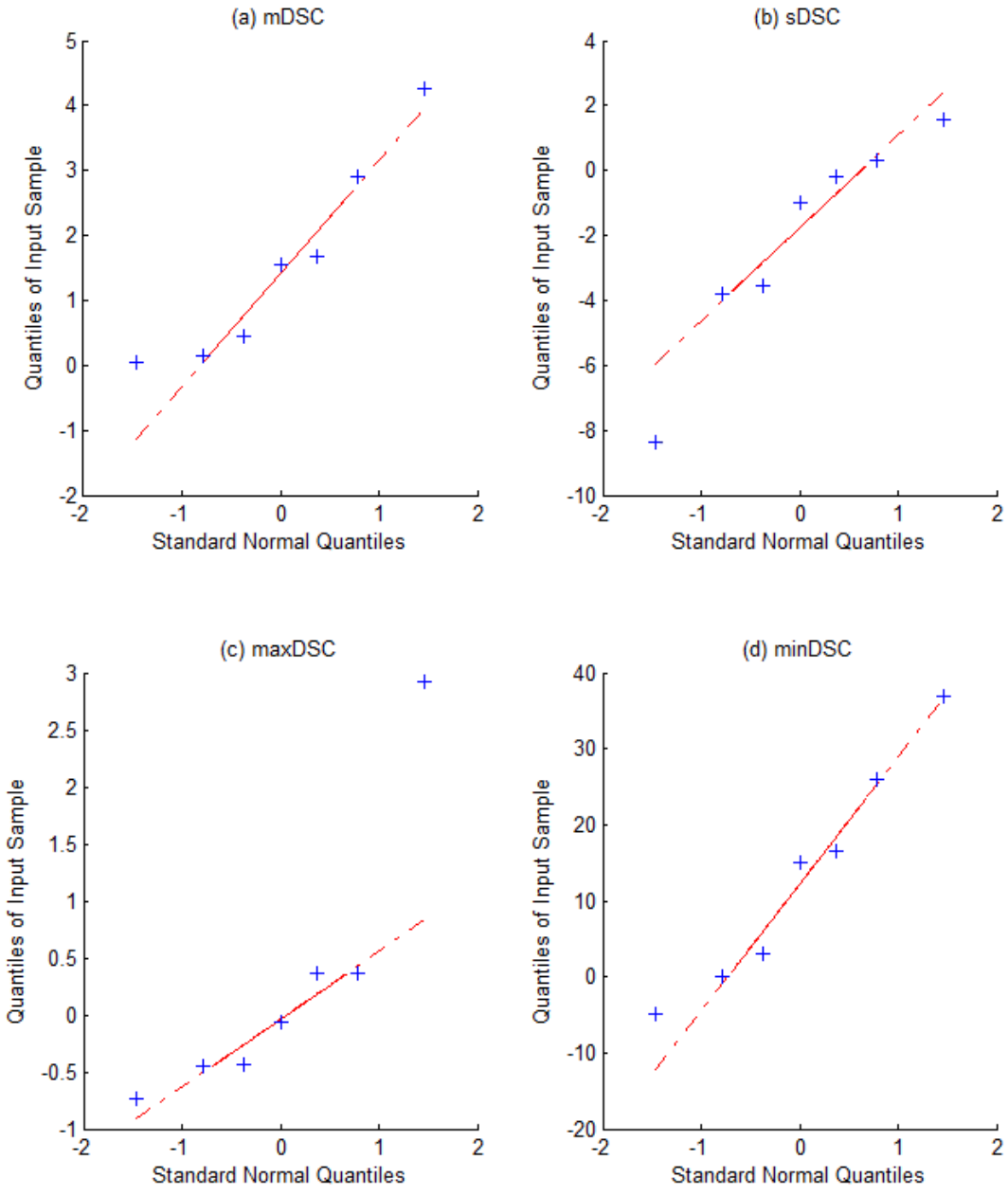

Fig. 4-5. Q-Q plots of the differences of (a) mDSC, (b) sDSC, (c) maxDSC, and (d) minDSC obtained without and with the elasticity penalty.

4.4 Discussions

It was proven that the elasticity penalty helped the B-spline DIR to avoid large misalignments that can be obtained without penalty under some of the parametric settings. Specifically, while almost no improvement was found on the highest accuracy by using the elasticity penalty, the B-spline DIR without penalty failed to align the muscle tissue depending on the parameter selection. This correction of large misalignments resulted in improvement of 1.6 % ($p < 0.05$) in the overall accuracy across the registration parameters associated with the image metric and optimization algorithm used. It should be noted that 1.6 % improvement achieved in the overall accuracy cannot be interpreted as substantial change in terms of DSC. Rather, relatively large improvement in DSC (> 10 %) was obtained under 8 parametric settings out of 108, showing the major impact of using the elasticity penalty.

In this study, DSC was used as a quantification measure of the registration accuracy since no ground-truth DVF is given with CT and CBCT images for HN soft tissue region. However, it should be noted that DSC only represent the quality of aligning contours of region of interest. In other words, high value of DSC achieved by B-spline DIR does not guarantee high registration accuracy of the volumetric deformation inside the muscle region. To evaluate the accuracy of the volumetric deformation, which is required for the dose accumulation in adaptive radiation therapy, a rigorous evaluation may be necessary, for instance, using a finite element-based evaluation method [35].

There may be some other circumstances under which the elasticity penalty has more impact on the registration accuracy than the impact shown in this study, suggesting several future

studies. First, in the B-spline DIR of registering the muscle in this investigation, the final B-spline grid spacing was (8, 8, 4) times image voxel dimensions (approximately 10 mm in each direction), beginning from a coarser grid. This multi-resolution scheme might restrict the level of flexibility of the B-spline transformation. When a finer B-spline transformation is used and the multi-resolution DIR begins with relatively high-resolution images, the elasticity penalty may have a large impact on the resultant deformations. Second, possible problems may include the deformable image registration of lung images, in which usually large deformation occurs. Furthermore, the elasticity penalty may have a relatively large impact when incorporated into other DIR algorithms such as demons algorithm.

The variations of the DSC values (sDSC) depending on the parameter selection were calculated as 8.3 % vs. 6.1 % for the B-spline DIR without and with the elasticity penalty (Table 4-4). By fine-tuning the parameters, a DSC close to 90 % was achieved for aligning the muscle while the average DSC was around 80 %. These findings suggest that the registration accuracy is affected by the selection of registration parameters and thus the registration parameters are carefully chosen to a specific problem. While some of the parameters associated with the image similarity metric and optimization algorithm were considered in this study, other parameters may have influence on the registration accuracy.

A finite difference method was used to calculate the second-order derivatives of the displacement vector, which is represented using B-spline functions. The rationale behind this calculation is based on understanding of the characteristics of the B-spline transformation. Additional constraints imposed on the second-order derivatives (in general, any order derivatives)

may not be satisfied by the B-spline transformation. It may be better to impose constraints on the displacement vector field than on the derivatives. By using the finite different calculation, the elasticity penalty was calculated by using the displacement vector field only.

4.5 Conclusions

By using the elasticity penalty, the accuracy of the B-spline DIR of the sternocleidomastoid muscle was improved on average across the registration parameters associated with the image metric and optimization algorithm. The overall accuracy (DSC) was improved because the elasticity penalty corrected the deformations with relatively low DSCs obtained by the B-spline DIR without penalty.

Chapter 5. Finite Element Head and Neck Model as a Supportive Tool for Deformable Image Registration

5.1 Overview

A finite element (FE)-based evaluation method was developed for the accuracy evaluation of the B-spline deformable image registration (DIR) of head and neck (HN) patient images. Useful aspects of the FE HN model include the ability to produce realistic deformations (similar to those seen in patients over the course of radiation treatment), and a rational means of generating new configurations, e.g., via the application of displacement and/or force boundary conditions. FE HN models were constructed based on cone-beam computed tomography (CBCT) images of HN cancer patients. For the FE analysis using the models, the skeletal elements were modeled as homogeneous rigid material and the surrounding tissue was modeled as homogeneous, linear elastic material. The developed FE model was capable of generating realistic deformations that are strain-free for the skeletal elements and of creating new configurations of the skeletal system with the surrounding tissues reasonably deformed. The FE models were also used to evaluate the accuracy of the B-spline DIR of five cervical vertebrae (C1 to C5). The results suggest that the FE models have a potential to provide a way of evaluating the accuracy of DIR by producing ground-truth displacement vector field (DVF) and correspondingly simulated images.

5.2 Methods

5.2.1 Preliminary test of a FE model under displacement/force boundary conditions

A FE head and neck model was constructed based on a head and neck cone-beam CT scan with an image dimension of 384 × 384 × 72 (0.651 × 0.651 × 2.5 mm^3 pixel dimension). First, voxels were automatically classified into 15 subsets according to the intensity values: 7 bony structures, 5 discs, 2 mandibular joints, and 1 class for the surrounding tissue. The discs were manually segmented based on a published study [47]. These discs and the joints connect the skull, mandible, and cervical vertebrae together. Manual modifications were applied on these voxel groups in order to make sure that there is no hole inside a structure or no isolated voxel outside the structure. These classified and refined voxel groups were converted to surface models (3-node triangular meshes). For the segmentation and surface model creation, a commercial software package (*Mimics 14*, Materialise Inc., Ann Arbor, MI), was used.

These triangular surface meshes were then converted to 4-node tetrahedral meshes. During this volumetric mesh generation, all the surface models were connected so that any two surfaces share all the nodes at the interface (*HyperMesh 10.0*, Altair Engineering Inc., Troy, MI). In other words, this can be interpreted that continuity conditions were imposed on the DVF at the interfaces between any two difference regions. The final FE model, shown in Fig. 5-1, was composed of 49731 nodes and 270382 elements.

As an example of the possible applications of the FE head and neck model, a deformation analysis was performed on the model under a set of displacement boundary conditions. For this

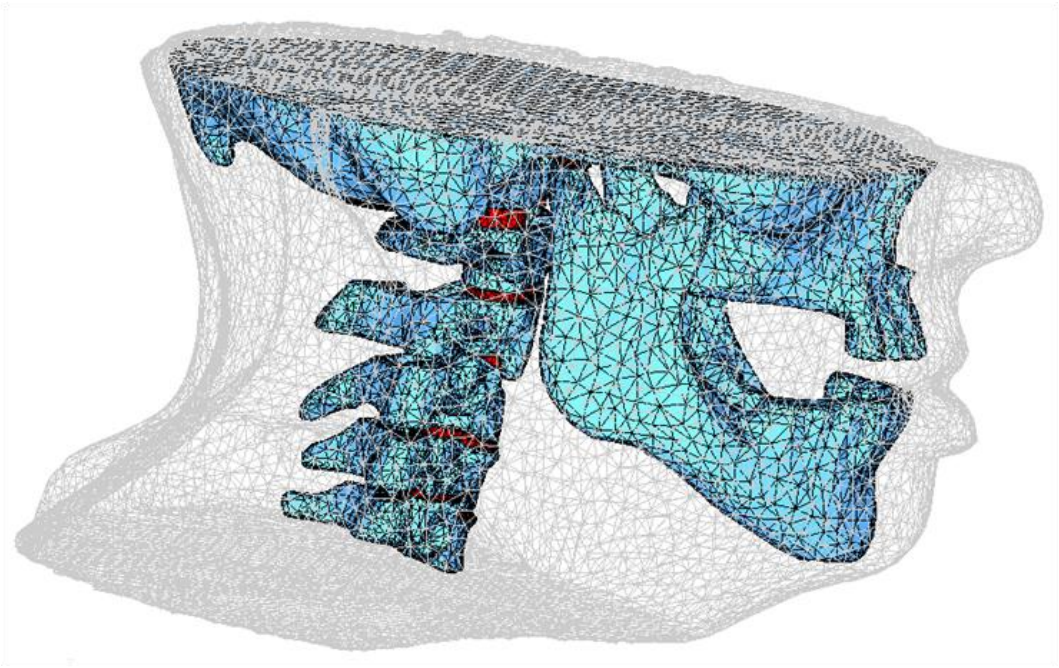

Fig. 5-1. Illustration of a FE head and neck model, in which bony elements, such as cervical vertebrae, mandible, and skull, are mechanically connected by intervertebral discs.

analysis, individual displacement boundary conditions were extracted from each of the surface pairs of the skull, mandible, and cervical vertebrae on two cone-beam CT scans which were taken at different treatment sessions. Specifically, 4 × 4 transformation matrices were obtained by using a surface registration algorithm (STL Registration, *Mimics 14*, Materialise Inc., Ann Arbor, MI). These transformation matrices were then used to calculate DVFs. Given these displacements as boundary conditions, a DVF was calculated by FE analysis using a commercial software package (*ABAQUS 6.10*, Simulia Corp, Northville, MI). Values of Young's modulus and Poisson's ratio (Table 5-1) were taken from previous studies [48-49].

Table 5-1 Mechanical properties used for bone, disc, and soft tissue in the FE head and neck models.

Material	Young's modulus (MPa)	Poisson's ratio
Bone	12000.0	0.29
Disc	3.4	0.40
Soft tissue	1.8	0.49

As the skeletal elements in the FE model were interconnected, a simple means of phantom reconfiguration can be achieved via application of a small number of force vectors. As an example, forces applied to the mandible and C5 as shown in Fig. 5-2. To reflect the condition of patient positioning at treatment (i.e. to restrict the transformation to the deformation about the

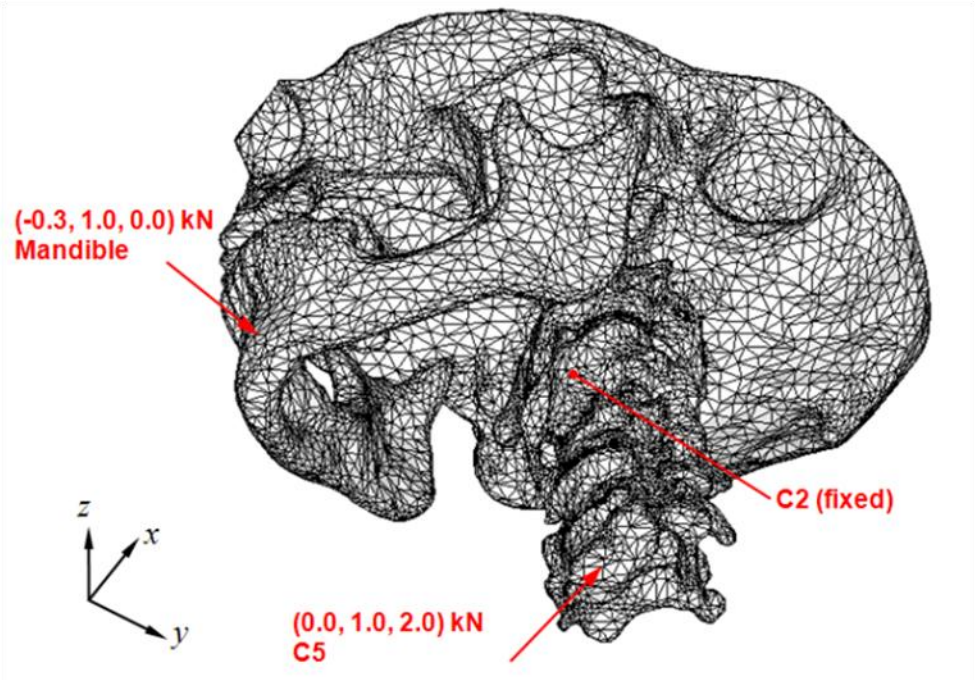

Fig. 5-2. Illustration of a set of force boundary conditions applied to the mandible and fifth cervical vertebra.

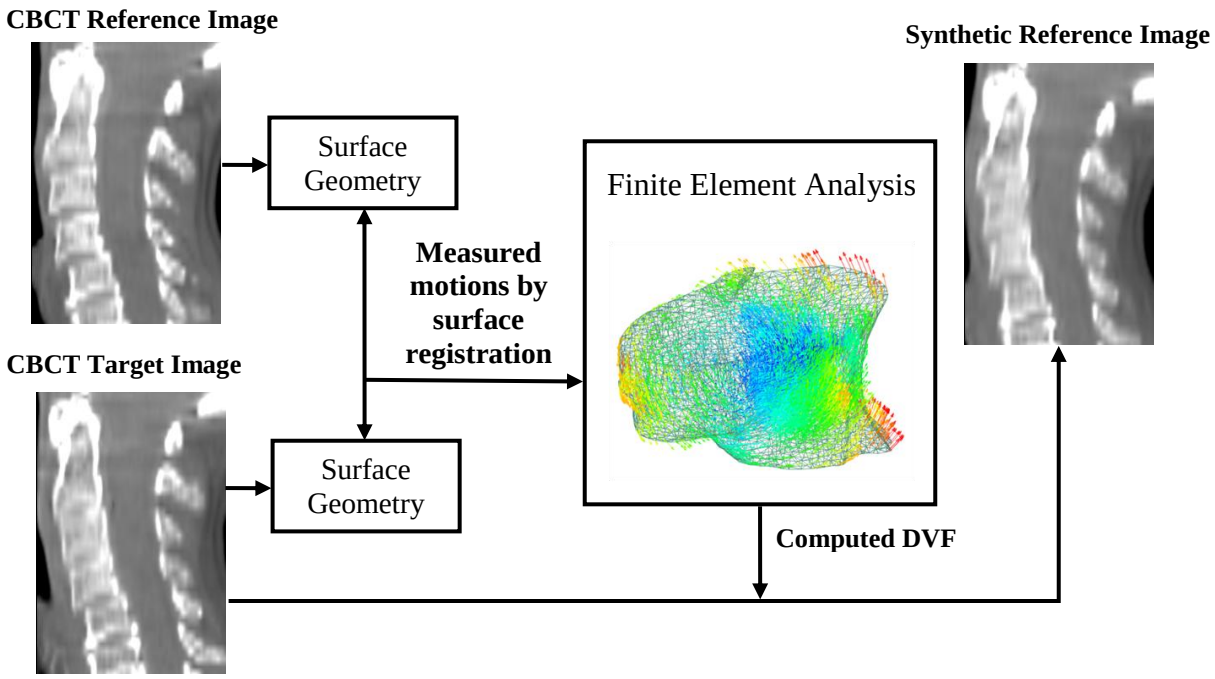

Fig. 5-3. Schematic description of FE-based generation of synthetic reference image and DVF (considered as the ground-truth DVF).

treated configuration of the patient), zero displacement on 4 points on the C2 vertebral body were imposed as displacement boundary conditions for this method. By the combination of force and displacement boundary conditions, a new phantom configuration was obtained by the FE analysis using *ABAQUS 6.10*.

5.2.2 Application to the evaluation of B-spline deformable image registration accuracy

Five FE HN models were constructed and used for the B-spline DIR of five cervical vertebrae, similar to the problem addressed in Chapter 3. The overall flow for the FE-based accuracy evaluation is illustrated in Fig. 5-3. First, the translation and rotation of the cervical

vertebrae were measured by registering the surface models constructed from the CBCT image pairs. The measured motions were then applied to the finite element model as displacement boundary conditions for the five cervical vertebrae. Finally, the synthetic reference images were generated by deforming the target CBCT images with the DVFs generated by the finite element analysis, which is considered as the ground-truth DVFs in the following tests. Then, the B-spline DIR was performed on the 25 sets of the synthetic reference and target CBCT images with the ground-truth DVFs generated by FE models. The B-spline DIR was performed without any penalty, and with the orthonormality-based rigidity penalty and the distance-preserving rigidity penalty (see Chapter 3 for both penalties).

In this study, the DIR with multi-resolution B-spline was implemented using the Insight Segmentation and Registration Toolkit (ITK) [44]. The B-spline DIR was set to begin with low-resolution image which was down-sampled by a factor of 4 in the left-right (LR) and anterior-posterior (AP) directions, not sampled in the inferior-superior (IS) direction. Then, the resolution of the reference and target images were doubled after each levels of registration was finished. The sum of the squared difference of image intensity [50], one of the most popular metrics was used to represent dissimilarity between the reference and target CBCT images.

5.2.2.1 Measurement of rigid motions: segmentation, surface model construction, and surface registration

In order to generate the synthetic reference images though FEM, one reference image and 5 target images for each of 5 patients were subject to segmentation and surface model generation.

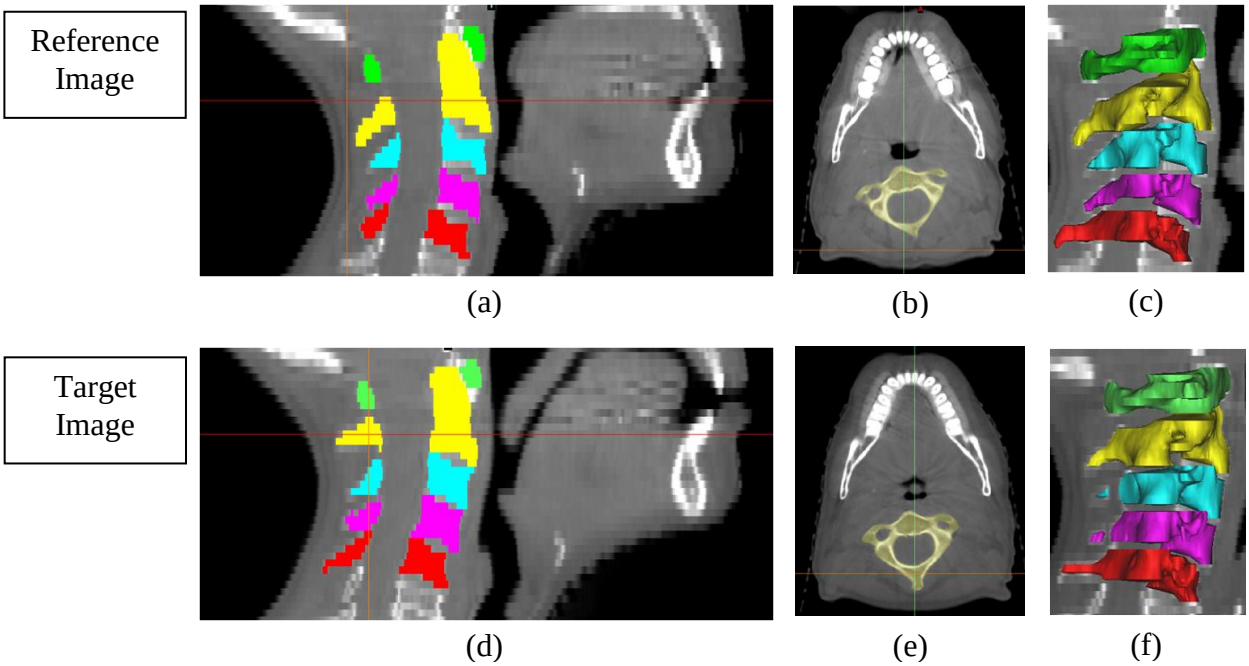

Fig. 5-4. Results of segmenting and constructing surface models for the five cervical vertebrae represented in a pair of reference and target CBCT images of a patient: (a), (d) labeled voxels for the cervical vertebrae overlaid on the sagittal cut, (b), (e) labeled voxels for the C2 vertebra overlaid on the axial cut, and (c), (f) surface models constructed for the vertebrae.

Voxels that belong to the five cervical vertebrae were automatically segmented by thresholding intensity values on both the reference and target images, and manual modifications were applied for separating each vertebral body from neighboring ones. Final segmentation results are illustrated in Fig. 5-4 (a), (b), (d), and (e). The segmented voxel sets were then converted to the corresponding surface models as shown in Fig. 5-4. (c) and (f). Rigid motions of the cervical vertebrae were measured by the aforementioned surface registration algorithm (see also Chapter 3.2.4.1).

5.2.2.2 Generation of the computed DVFs and synthetic reference images via finite element analysis

The surface models from the reference image were converted to volumetric meshes for finite element modeling. The rigid motions measured by the surface registration were used as displacement boundary conditions. Finite element analysis calculated the DVFs in the neck region (shown in Fig. 5-3), which were considered as the ground-truth DVFs in the following tests. Synthetic reference images were generated by applying the computed DVFs to each of 25 target CBCT images from 5 patients.

5.2.2.3 Evaluation of registration accuracy

For the evaluation of the accuracy of the B-spline DIR, three quantitative measures were calculated: registration error, transformation, and the Procrustes distance (see Chapter 3.2.4.2).

5.3 Results

5.3.1 FE analysis under displacement boundary conditions

Figure 5-5 (a) shows the resultant DVF overlaid on an axial cut of CBCT image volume on which the construction of the FE model was based. It demonstrates the transformation resultant from a translation as well as rotation of the proximal vertebral body. In addition, the original configuration was transformed into a new configuration as can be seen in Fig. 5-5 (b)

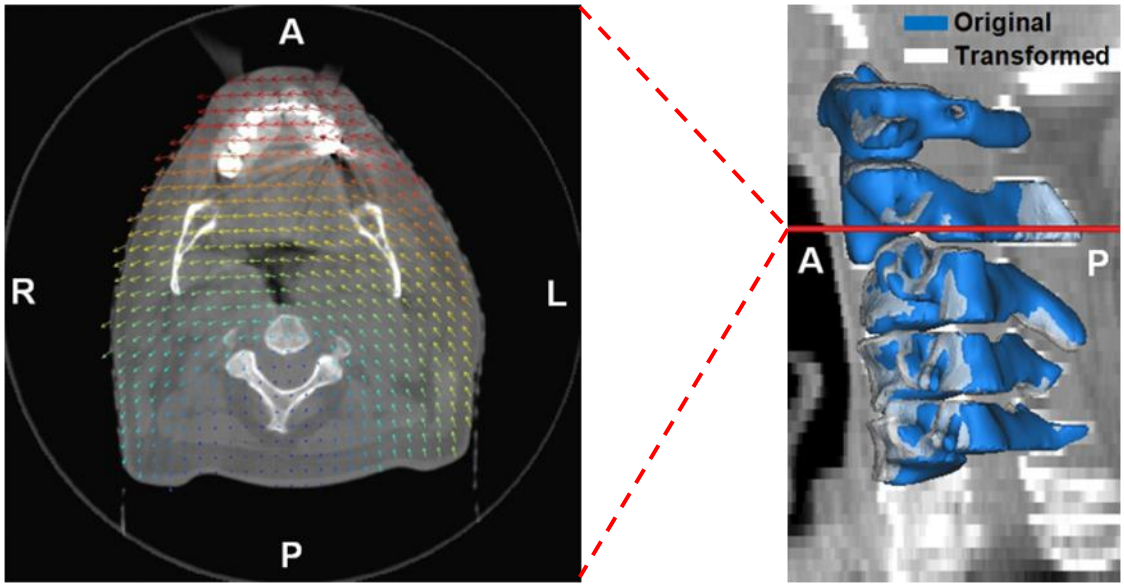

(a) (b)

Fig. 5-5. Results of the FE analysis under displacement boundary conditions: (a) the displacement vector field overlaid on an axial plane of the cone-beam CT image volume on which the model was constructed (scaled), (b) the original and deformed geometries of the cervical vertebrae (C1-C5) with the level of the CT slice shown in (a) annotated (A = anterior, P = posterior, L = left, R = right)

that shows the original and transformed surfaces of the cervical vertebrae. The maximum displacement magnitude of all nodal points was 7.0 mm.

The accuracy for the FE analysis was verified by manually locating 8 landmark pairs on both images; these landmark points are located at the midpoint of the bilateral foramina of the cervical vertebrae. Differences between the displacements measured using the landmarks and those generated by the FE analysis were $(0.2 \pm 0.3, -0.2 \pm 0.4, -0.1 \pm 1.0)$ [mm]. This result shows that the FE analysis correctly transformed the original configuration into the target configuration. The strain components calculated on the bony elements were close to zero, indicating a realistic skeletal deformation was resulted.

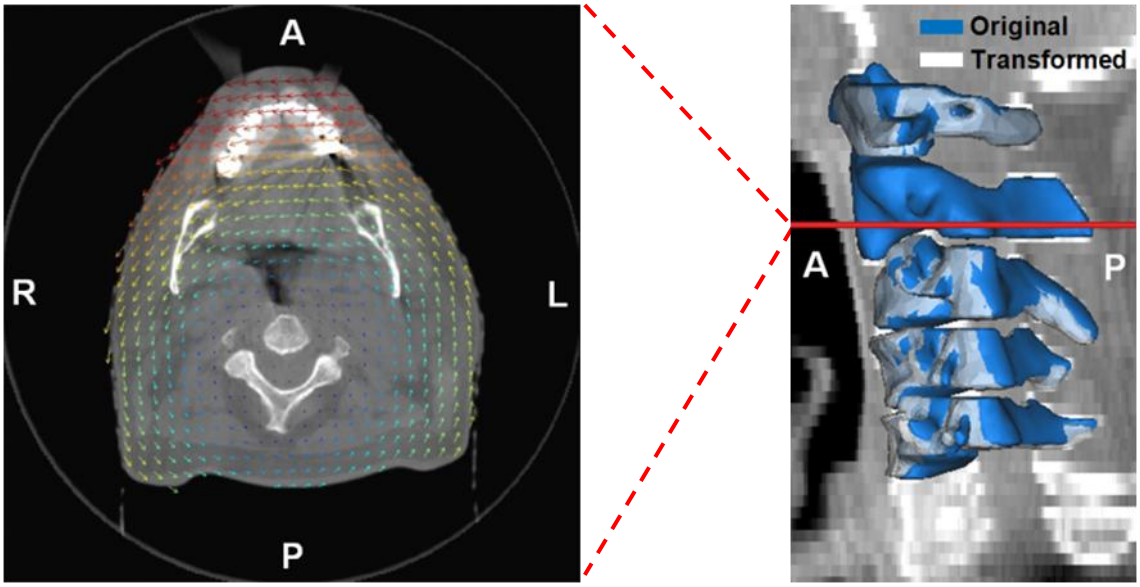

(a) (b)

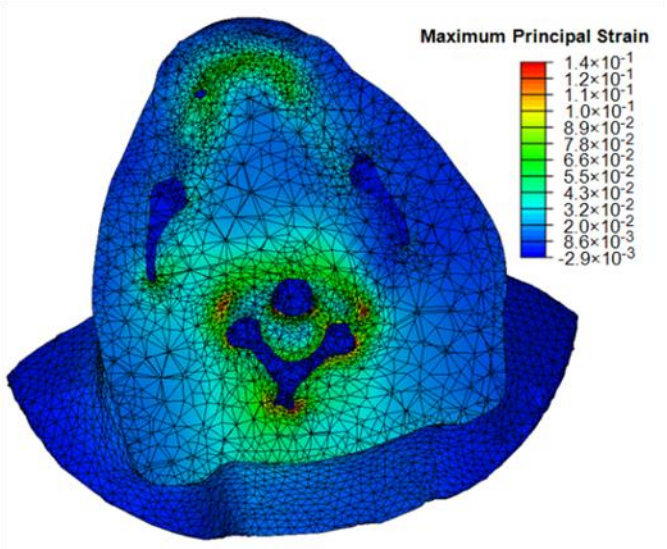

(c)

Fig. 5-6. Results of the FE analysis under a combined set of force and displacement boundary conditions: (a) the displacement vector field overlaid on an axial plane of the cone-beam CT image volume on which the model was constructed (scaled), (b) the original and transformed geometries of the cervical vertebrae (C1-C5) with the level of the CT slice shown in (a) annotated, (c) the maximum principal strain field shown on the deformed geometry (A = anterior, P = posterior, L = left, R = right)

5.3.2 FE analysis under force and displacement boundary Conditions

Figure 5-6 shows an example of force-based model reconfiguration with displacement boundary conditions for C2. Although, in this analysis, forces were applied only to the mandible and C5, the other bony elements accordingly moved and deformation also occurred in the surrounding tissue. The DVF is overlaid on an axial plane of the CBCT image in Fig. 5-6 (a). The original and deformed surfaces of the cervical vertebrae are compared in Fig. 5-6 (b). The values of the maximum principal strain are plotted on the deformed geometry in Fig. 5-6 (c). Nearly zero strains calculated in the regions of the mandible and C4 clearly show that the FE model is able to produce skeletal deformations via FE analysis under force and displacement boundary conditions.

5.3.3 Accuracy evaluation of deformable image registration of five cervical vertebrae

Figure 5-7 shows comparisons of the DVFs from registrations (blue) with the ground-truth DVF (red). Figure 5-8 shows the comparison of the synthetic reference image and the deformed target images generated by applying the DVFs from the registration. The DVFs without and with rigidity penalty (either orthonormality-based or distance-preserving) transformed bone voxels in the target image visibly close to those in the reference image, indicating that all image registrations performed reasonably well in terms of intensity matching. However, the detailed examination of the DVFs in Fig. 5-7 reveals that the B-spline DIR without penalty resulted in the deformation maps that lacked biomechanical consistency in the skeletal elements, where considerable local deformation was observed in the vertebral bodies.

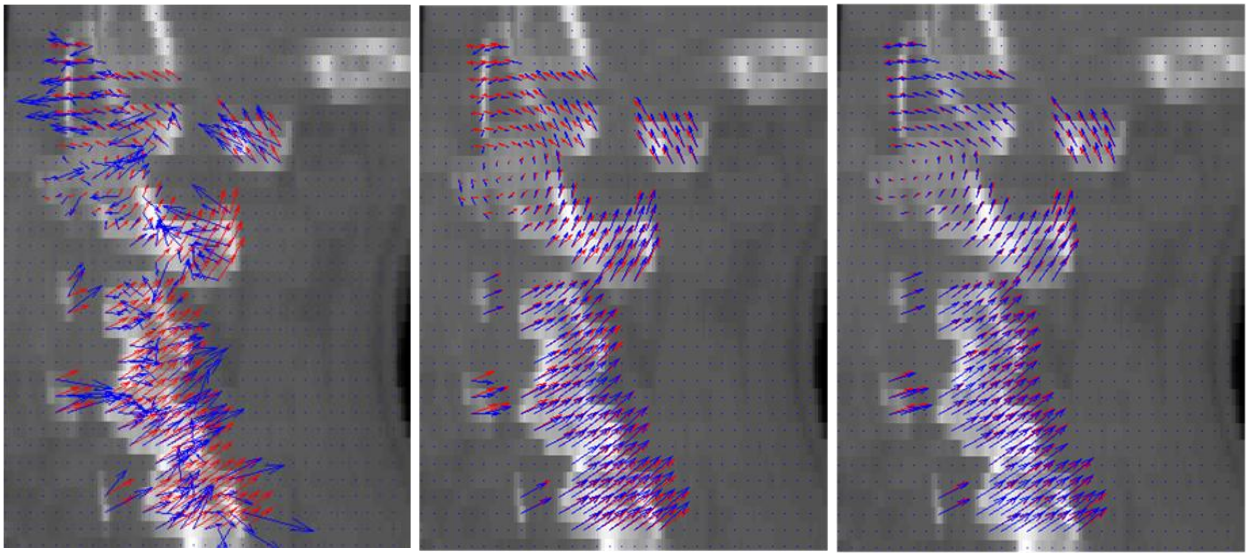

(a) (b) (c)

Fig. 5-7. Comparison of the DVFs (blue) by the B-spline DIR (a) without penalty, (b) with the orthonormality-based rigidity penalty, and (c) with the distance-preserving rigidity penalty to the ground-truth DVF (red).

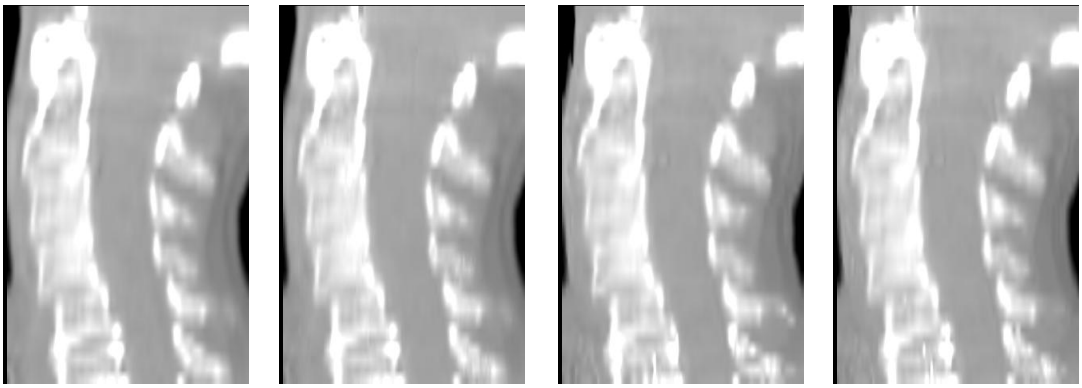

(a) (b) (c) (d)

Fig. 5-8. Sagittal cuts of (a) a synthetic reference image and the target images deformed by the DVFs (shown in Fig. 5-7) by the B-spline DIR (b) without penalty, (c) with the orthonormality-based rigidity penalty, and (d) with the distance-preserving rigidity penalty.

The displacement components in the AP and IS directions plotted in Fig. 5-9 (a) and (b) show how the resultant DVFs with the orthonormality-based and distance-preserving rigidity

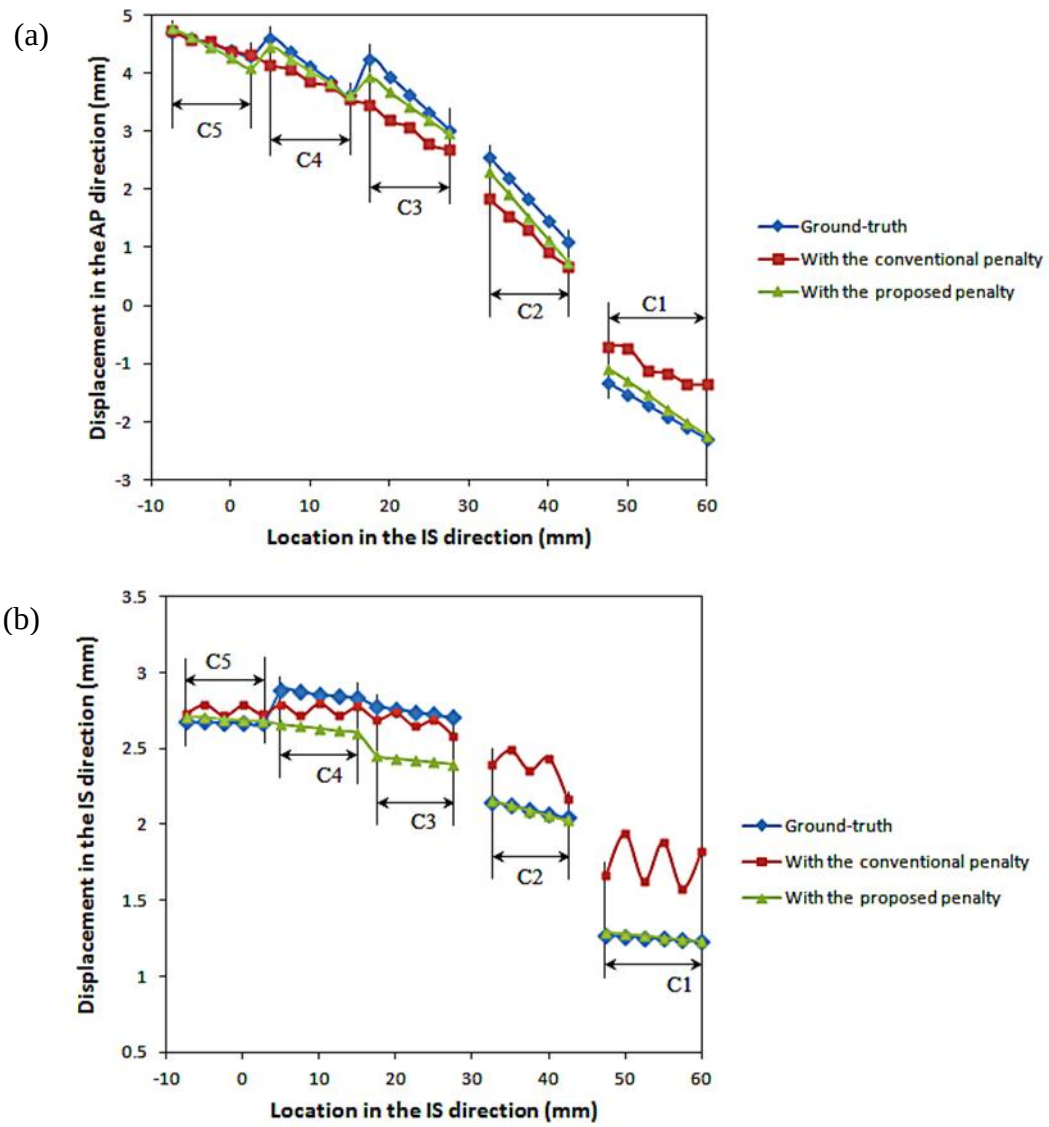

Fig. 5-9. Plots of the displacement vector components in the (a) AP and (b) IS directions across the vertebral bodies.

penalties recovered the ground-truth DVF exhibiting abrupt changes across the vertebrae. While the DVF obtained with the conventional orthonormality-preserving penalty was over-smoothing

Table 5-2 Registration errors between the DVFs in the LR, AP, and IS directions of the five cervical vertebrae without and with the rigidity penalties.

		Intensity-based	Orthonormality-preserving	Distance-preserving
Registration Error (mm)				
	Mean magnitude	(1.91, 2.13, 1.68)	(0.13, 0.17, 0.26)	(0.08, 0.10, 0.12)
	Standard deviation	(2.54, 2.77, 2.26)	(0.18, 0.24, 0.34)	(0.12, 0.14, 0.16)

Table 5-3 Comparison of the transformation errors and Procrustes distance between the DVFs without penalty and with the rigidity penalties.

		Intensity-based	Orthonormality-preserving	Distance-preserving
Translation (mm)				
	Mean magnitude	(0.55, 0.87, 0.57)	(0.07, 0.09, 0.12)	(0.04, 0.05, 0.08)
	Standard deviation	(0.61, 1.07, 0.73)	(0.08, 0.12, 0.15)	(0.05, 0.06, 0.10)
Rotation (°)				
	Mean magnitude	(2.12, 1.03, 1.31)	(0.59, 0.31, 0.32)	(0.46, 0.22, 0.19)
	Standard deviation	(2.33, 1.33, 1.65)	(0.74, 0.39, 0.42)	(0.67, 0.29, 0.25)
Procrustes distance (mm)		3.52 (0.36)	0.30 (0.11)	0.12 (0.07)

or oscillatory, the DVF obtained with the proposed distance-preserving penalty faithfully recovered the acute changes in the displacement.

The mean magnitudes and standard deviations of the registration errors are summarized in Table 5-2. Compared to the mean magnitude of (1.91, 2.13, 1.68) mm and (0.13, 0.17, 0.26) mm obtained by the B-spline DIR without rigidity penalty and with the orthonormality-based

rigidity penalty, the mean magnitude of registration error was reduced to (0.08, 0.10, 0.12) mm with the distance-preserving rigidity penalty.

The mean magnitudes and standard deviations of the transformation errors are summarized in Table 5-3. The proposed distance-preserving rigidity penalty outperformed the existing orthonormality-based rigidity penalty: (0.04, 0.05, 0.08) mm vs. (0.07, 0.09, 0.12) mm for translation and (0.67, 0.29, 0.25) ° vs. (0.74, 0.39, 0.42) ° for rotation. The Procrustes distances for the proposed distance-preserving rigidity penalty were less than those for no rigidity penalty and the existing orthonormality-based rigidity penalty: 0.12 mm (0.07 mm) vs. 3.52 (0.36 mm) and 0.30 mm.

5.4 Discussion

The objective of this work was to develop a FE head and neck model as a supportive tool for DIR research in Radiation Therapy. The FE model can provide realistic deformations in the neck region. As a computational head and neck phantom, the model provides a tool for the evaluation of DIR accuracy. The deformations obtained by the FE model can be used to simulate images with the effects of realistic variations in neck translocation and articulation. These ground truth deformations and corresponding image volumes provide a set of tools to examine the accuracy of DIR algorithms.

The registration results obtained with the 25 sets of the synthetic reference and target CBCT images showed similar trends with those obtained with the 25 sets of the CT and CBCT

images shown in Chapter 3. This finding indicated that the finite element-based evaluation method was successfully implemented for the B-spline DIR of the cervical vertebrae.

It is noteworthy to mention differences in the B-spline DIR accuracy of the five cervical vertebrae shown in Tables 3-3 and 5-2. The registration error in the IS direction was larger for the deformations obtained with the real image pairs (Table 3-3) than for those with the synthetic/real image pairs (Table 5-2): 0.38 mm vs. 0.12 mm with the proposed distance-preserving rigidity penalty. The reasons for this discrepancy can be found from differences between the two different studies. The ground-truth DVFs for the study in Chapter 3 include errors of measuring the rigid motions of the five cervical vertebrae via the surface registration. On the other hand, in the FE-based evaluation of the registration accuracy in this chapter, the ground-truth DVFs do not have any error since the synthetic reference images were simulated via the FE analysis. Another difference, which may have an impact on the accuracy, is in the type of the DIR problems. While the CT and CBCT images, used in the study in Chapter 3, have different intensity histograms (so a mutual information works properly), the B-spline DIR problem in the study in this chapter is a problem of aligning two images of same kind.

The current FE model can be improved by considering other soft tissues such as muscles in the neck region. With the use of nonlinear elastic material properties, the deformation in the surrounding tissues may be more reasonably produced. The use of the FE-based evaluation method presented in this study is limited to the evaluation of the registration accuracy between the images acquired with the same imaging modality. In order to use the FE models for the

accuracy evaluation of multimodal image registration problems, a special technique should be used to deform the target images to generate synthetic reference images.

One of the challenging tasks for the construction of the FE model was to segment the discs which are, in general, not visually distinguishable in CT images. The geometries of the discs in the model may have an influence on the value of the elastic stiffness of the discs. However, this may not remarkably degrade the ability of the model to generate realistic deformations; assigning large values of Young's modulus to the skull, mandible, and cervical vertebrae (Table 5-1) guarantees the rigid body motions of those components.

Another limitation of the current model is that the geometry of the skull is simplified for the sake of convenience in volumetric meshing. While increasing the potential for non-physical deformations, the overall rigidity of the skull as a unit suggests that simplifying its shape somewhat may have minimal influence on the propagation of forces and displacements to surrounding anatomy.

Furthermore, physiological changes such as weight loss, tumor growth, and tumor response to radiation have not been taken into consideration. Incorporating a mathematical model of tumor growth and response may further aid the utility of this model for enhancing and investigating image registration accuracy.

5.5 Conclusions

The FE HN models developed successfully generated realistic deformations similar to those seen from the patients (e.g. no local deformation in skeletal elements). The FE-based evaluation framework was successfully used to evaluate the accuracy of the B-spline DIR of five cervical vertebrae.

Chapter 6. Summary

6.1 Summary

The objective of the thesis is 1) to improve the accuracy of the B-spline deformable image registration (DIR) of head and neck (HN) CT/CBCT images by developing penalties, and 2) to develop a finite element (FE)-based evaluation method of the registration accuracy.

The distance-preserving rigidity penalty improved the accuracy of the B-spline DIR of five cervical vertebrae in the neck region and outperformed the existing orthonormality-based rigidity penalty for this particular problem, in which multiple rigid bodies are tightly located, as discussed in Chapter 3. By using the elasticity penalty, large misalignments, which resulted from the B-spline DIR without the aid of the penalty and under some of the parametric settings, were corrected (Chapter 4). The deformations with low DSC values (< 20 %) were corrected by using the elasticity penalty. A finite element (FE)-based evaluation method was developed by constructing the FE models, which are capable of generating realistic deformations similar to those seen from HN patients. The FE-based method was utilized to rigorously evaluate the accuracy of the B-spline DIR of five cervical vertebrae.

6.2 Future Work

Testing on a sufficient sample size of, for instance, 30 patients will need to be performed as a future study in order to strongly support the findings in this thesis. A limitation of the dissertation is that B-spline DIR was performed on the image data sets of a few HN patients (5 patients in Chapters 3 and 5, and 2 patients in Chapter 4). For the study in Chapter 3, these small sample numbers may be justified with the finding that the rigid motions measured by a surface registration (seen from 5 HN patients) were comparable to those measured with the image data sets of 23 HN patients in Ahn *et al*. [43]. In addition, immobilizing a HN patient by using thermoplastic mask is a current clinical routine that prevents large setup error. In addition, relatively large displacements of lower cervical spine and rotation of C1 vertebra, typical motions seen from the HN patients who are adequately immobilized and positioned in reference to C2 position, were taken into consideration in this dissertation. However, testing with additional patients samples will help sufficiently cover the range of variability that will be encountered in clinical practice. For instance, a HN patient with osteoporosis may undergo bone deformation when positioned, possibly affecting the efficacy of the proposed rigidity penalty.

The impact of registration parameters was considered in the study with the elasticity penalty (Chapter 4) while not in the study with the rigidity penalty (Chapter 3). This can be explained by the difference in the impact of the penalty terms on the performance of the B-spline DIR. The proposed distance-preserving rigidity penalty could prevent the bone warping of five cervical vertebrae, in other words, correct physically unreasonable deformation. On the other hand, the ability of the elasticity penalty to prevent nonphysical deformation could not be proven

because there was no method to evaluate the accuracy of volumetric deformation. Instead, by performing B-spline DIR with various parameter selections, it was proven that the elasticity penalty could help the B-spline DIR to avoid large misalignments obtained under some of the parametric settings. Although the main contributions of the penalty terms to the B-spline DIR are different, the impact of registration parameters should be investigated in a future study with the rigidity penalty terms.

The impact of the elasticity penalty should be further investigated in future work. First, the elasticity penalty needs to be tested for the B-spline DIR of other muscles in the HN region. However, in this registration problem, it will be challenging to evaluate the registration accuracy since it is hard both to segment other muscles and to find ground-truth displacement vector fields (DVFs). Therefore, this future study should be supported by an improved evaluation method, for instance, FE-based evaluation method. Second, the impact of the elasticity penalty needs to be verified with an additional test either on images of another region or with another DIR algorithm such as a demons algorithm. The deformations covered by the multi-resolution B-spline DIR for the sternomastoid muscle in the HN region were smooth, so that the elasticity penalty may not be used to correct physically unreasonable deformations. A potential impact of the elasticity penalty to regularize physically unreasonable deformations should be investigated in a future study.

The distance-preserving rigidity penalty (Chapter 3) and the elasticity penalty (Chapter 4) were separately used in the B-spline DIR of HN CT/CBCT image pairs. Although the impact of each of the penalty terms was investigated, it is still uncertain how those terms will work when

combined with each other. It should be investigated as a future study whether the two penalty terms have the same impact compared to when each was individually tested. In addition, the planning CT images were cropped so that the images include the regions, where the registration accuracy was evaluated, i.e. five cervical vertebrae in Chapter 3 and sternomastoid muscle in Chapter 4. In order for the findings from the dissertation to have clinical relevance, the B-spline DIR should be tested with a sufficiently wide image portion that contains all important structures such as tumor volumes and normal organs-at-risk.

In addition, this thesis mainly focused on B-spline DIR of planning CT and treatment CBCT images. However, this is only a special case of HN RT, in which a patient is examined with a CBCT scanner on a daily basis. In contrast to the CBCT-guided RT, a patient is scanned with a conventional CT scanner a few times, e.g. weekly or daily, during the course of RT in another type of adaptive radiation therapy [7, 51]. In this case, CT-CT DIR needs to be performed instead of CT-CBCT DIR. As a future study, it is of interest to evaluate the impact of the penalty terms on the accuracy of the CT-CT B-spline DIR.

The FE HN models were used only for the evaluation of the B-spline DIR of rigid regions such as cervical vertebrae. In order for the current FE models to be used to evaluate the deformations in soft tissue in the HN region, the models should be further improved. For instance, a simple way to improve the model will be applying different mechanical properties for HN soft tissue regions in a relation to the image intensity values of each region. Two main types of soft tissue in the HN region are muscle and fat, each of which has an own range of the image intensity value and corresponding mechanical properties. This approach does not require to

construct surface meshes for each of the soft tissue regions and to consider sliding motions between muscles. Simply assigning different mechanical properties to the FE elements of each soft tissue region will provide more realistic deformations than the case of treating the entire HN soft tissue region as a homogeneous, elastic material. Although it is hard to segment all of HN muscles and other soft tissues from CT scans, with the aid of atlas, it could be possible to construct a realistic FE model, in which some of sliding motions are taken into account. With physically realistic deformations generated with the aforementioned improvements, the accuracy of DIR algorithms can be rigorously evaluated in the HN soft tissue region as well as in the skeletal regions.

6.3 Thesis Contributions

6.3.1 Scholarly Contributions

This dissertation aims at improving the accuracy of the B-spline DIR of HN CT images by introducing penalty terms from biomechanical principles and developing a FE-based evaluation method for DIR accuracy in HN region. The scholarly contributions of this dissertation can be summarized as follows:

- **Distance-preserving rigidity penalty:** Development of a rigidity penalty which is designed to preserve inter-voxel distances within each rigid region. This penalty term outperformed an existing rigidity penalty that preserves the orthonormality of the

deformation gradient tensor for the B-spline DIR of tightly-located multiple skeletal elements such as five cervical vertebrae in HN region. The orthonormality-based rigidity penalty cannot fully prevent the bone warping problem when multiple rigid regions exist in close proximity. The development of the proposed penalty was based on a fundamental understanding of the B-spline DVF, which is represented as a linear combination of B-spline basis functions. Imposing constraints on the derivatives of the DVF (e.g. the orthonormality condition), not on the DVF directly, cause the B-spline DIR to be over-constrained, thus resulting in over-smoothness or oscillation in the DVF.

- **Elasticity penalty:** Use of a penalty that preserves linear elasticity within sternomastoid muscle during B-spline DIR of HN CT images. This study is a first effort to use a penalty within DIR of HN images. The penalty term is designed to prevent the resultant DVFs from violating the static equilibrium equations for linear elastic materials. By using this elasticity penalty, the overall workflow of the B-spline DIR can be improved by eliminating time-consuming parameter tuning processes. Using a finite difference method for the computation of the second-order derivatives of DVF, which is required to compute the penalty term, enabled to impose constraints on the DVF, avoiding possible issues with constraints on the derivatives.
- **FE-based evaluation of registration accuracy:** Development of a FE HN model that can be used to evaluate registration accuracy. An effort was made to generate ground-truth DVFs similar to those which can be seen from HN patients. Simulating

the FE model under the displacement boundary conditions, i.e. the rigid motions of skeletal elements measured by a surface registration, can generate physically reasonable DVFs. For instance, no local deformation occurs within the skeletal elements. Therefore, the B-spline DIR accuracy of five cervical vertebrae was successfully evaluated with the current FE model. This study provides a good starting point for the development of an advanced FE model which is capable of providing ground-truth DVFs that have a sufficient coverage of the HN region.

6.3.2 Societal Contributions

The outcome of the dissertation may contribute to successful treatment of HN cancer with radiation. The accurate deformation maps obtained by the B-spline DIR with the aid of the penalties can bring enhancement in detecting anatomical changes in healthy tissue regions surrounding tumor in a patient. Then, this enhancement will help accurately estimate the radiation dose delivered to the patient and determine whether the initial radiation treatment plan needs to be adjusted in response to the anatomical changes provided by the B-spline DIR. The FE HN models can support the development and research of DIR algorithms by providing realistic ground-truth DVFs, with which the registration accuracy of B-spline DIR algorithm can be rigorously evaluated before its use in the clinic setting.

References

[1] A. Jemal, R. Siegel, J. Xu, and E. Ward, "Cancer statistics, 2010," CA: A Cancer Journal for Clinicians **60** (5), 277–300 (2010).

[2] L. Xing, Q. Wu, Y. Yang, and A. Boyer, "Physics of IMRT," in *Intensity Modulated Radiation Therapy: a Clinical Perspective*, edited by A. J. Mundt and J. C. Roeske (B. C. Decker, Inc., Hamilton and London, 2005), pp. 20−52.

[3] J. L. Barker, A. S. Garden, K. K. Ang, J. C. O'Daniel, H. Wang, L. E. Court, W. H. Morrison, D. I. Rosenthal, K. S. C. Chao, S. L. Tucker, R. Mohan, and L. Dong, "Quantification of volumetric and geometric changes occurring during fractionated radiotherapy for head-and-neck cancer using an integrated CT/linear accelerator system," Int. J. Radiat. Oncol., Biol., Phys. **59** (4), 960–970 (2004).

[4] C. Lee, K. M. Langen, W. Lu, J. Haimerl, E. Schnarr, K. J. Ruchala, G. H. Olivera, S. L. Meeks, P. A. Kupelian, T. D. Shellenberger, and R. R. Mañon, "Evaluation of geometric changes of parotid glands during head and neck cancer radiotherapy using daily MVCT and automatic deformable registration," Radiother. Oncol. **89**, 81−88 (2008).

[5] C. Lee, K. M. Langen, W. Lu, J. Haimerl, E. Schnarr, K. J. Ruchala, G. H. Olivera, S. L. Meeks, P. A. Kupelian, T. D. Shellenberger, and R. R. Mañon, "Assessment of parotid gland dose changes during head and neck cancer radiotherapy using daily megavoltage computed tomography and deformable image registration," Int. J. Radiat. Oncol., Biol., Phys. **71**, 1563−1571 (2008).

[6] W. Lu, G. H. Olivera, Q. Chen, M. Chen, and K. J. Ruchala, "Automatic re-contouring in 4D radiotherapy," Phys. Med. Biol. **51**, 1077−1099 (2006).

[7] T. Zhang, Y. Chi, E. Meldolesi, and D. Yan, "Automatic delineation of on-line head-and-neck computed tomography images: toward on-line adaptive radiotherapy," Int. J. Radiat. Oncol., Biol., Phys. **68**, 522−530 (2007).

[8] Q. Wu, Y. Chi, P. Y. Chen, D. J. Krauss, D. Yan, and A. Martinez, "Adaptive replanning strategies accounting for shrinkage in head and neck IMRT," Int. J. Radiat. Oncol., Biol., Phys. **75**, 924−932 (2009).

[9] M. Peroni, D. Ciardo, M. F. Spadea, M. Riboldi, S. Comi, D. Alterio, G. Baroni, and R. Orecchia, "Automatic segmentation and online *virtual*CT in head-and-neck adaptive radiation therapy," Int. J. Radiat. Oncol., Biol., Phys. **84**, e427−e433 (2012).

[10] T. Rohlfing, "Image similarity and tissue overlaps as surrogates for image registration accuracy: Widely used but unreliable," IEEE Trans. Med. Imaging **31**, 153−163 (2012).

[11] R. Kashani, M. Hub, J. M. Balter, M. L. Kessler, L. Dong, L. Zhang, L. Xing, Y. Xie, D. Hawkes, J. A. Schnabel, J. McClelland, S. Joshi, Q. Chen, and W. Lu, "Objective assessment of deformable image registration in radiotherapy: A multi-institution study," Med. Phys. **35**, 5944−5953 (2008).

[12] S. Nithiananthan, S. Schafer, A. Uneri, D. J. Mirota, J. W. Stayman, W. Zbijewski, K. K. Brock, M. J. Daly, H. Chan, J. C. Irish, and J. H. Siewerdsen, "Demons deformable registration of CT and cone-beam CT using an iterative intensity matching approach," Med. Phys. **38**, 1785–1798 (2011).

[13] N. Kirby, C. Chuang, and J. Pouliot, "A two-dimensional deformable phantom for quantitatively verifying deformation algorithms," Med. Phys. **38**, 4583−4586 (2011).

[14] J. Hou, M. Guerrero, W. Chen, and W. D. D'Souza, "Deformable planning CT to cone-beam CT image registration in head-and-neck cancer," Med. Phys. **38**, 2088−2094 (2011).

[15] S. Nithiananthan, K. K. Brock, M. J. Daly, H. Chan, J. C. Irish, and J. H. Seiwerdsen, "Demons deformable registration for CBCT-guided procedures in the head and neck: Convergence and accuracy," Med. Phys. **36**, 4755−4764 (2009)

[16] C. O. S. Sorzano, P. Thévenaz, and M. Unser, "Elastic registration of biological images using vector-spline regularization," IEEE Trans. Biomed. Eng. **52**, 652−663 (2005).

[17] M. Sdika, "A fast nonrigid image registration with constraints on the Jacobian using large scale constrained optimization," IEEE Trans. Med. Imaging **27**, 271−281 (2008).

[18] T. Rohlfing, C. R. Maurer, D. A. Bluemke, and M. A. Jacobs, "Volume-preserving nonrigid registration of MR breast images using free-form deformation with an incompressibility constraint," IEEE Trans. Med. Imaging **22**, 730−741 (2003).

[19] D. Loeckx, F. Maes, D. Vandermeulen, and P. Suetens, "Nonrigid image registration using free-form deformations with a local rigidity constraint," in *MICCAI*, Vol. 3216 Lecture Notes in Computer Science, 639−646 (Springer Verlag, Berlin/Heidelberg, 2004).

[20] D. Ruan, J. A. Fessler, M. Roberson, J. Balter, and M. Kessler, “Nonrigid registration using regularization that accommodates local tissue rigidity,” Proceedings of SPIE, **6144**, 346–354 (2006).

[21] M. Staring, S. Klein, and J. P. W. Pluim, “A rigidity penalty term for nonrigid registration,” Med. Phys. **34**, 4098−4108 (2007).

[22] A. Sotiras, C. Davatzikos, and N. Paragios, “Deformable image registration: A survey,” IEEE Trans. Med. Imaging **32**, 1153−1172 (2013).

[23] C. Broit, "Optimal registration of deformed images” (January 1, 1981). Dissertations available from ProQuest. Paper AAI8207933. http://repository.upenn.edu/dissertations/AAI8207933

[24] R. Bajcsy and S. Kovacic, “Multiresolution elastic matching,” Comput. Vision Graphics Image Process. **46**, 1−21 (1989).

[25] G. E. Christensen and H. J. Johnson, “Consistent image registration,” IEEE Trans. Med. Imaging **20**, 568−582 (2001).

[26] A. Al-Mayah, J. Moseley, S. Hunter, M. Velec, L. Chau, S. Breen, and K. K. Brock, “Biomechanical-based image registration for head and neck radiation treatment,” Phys. Med. Biol. **55**, 6491–6500 (2010).

[27] A. W. C. Lee, J. A. Schnabel, V. Rajagopal, P. M. F. Nielsen, and M. P. Nash, “Breast image registration by combining finite elements and free-form deformations,” in Digital Mammography: 10th International Workshop, Vol. 6136 Lecture Notes in Computer Science, 736−743 (Springer Verlag, Berlin/Heidelberg, 2010).

[28] K. K. Brock, M. B. Sharpe, L. A. Dawson, S. M. Kim, and D. A. Jaffray, “Accuracy of finite element model-based multi-organ deformable image registration,” Med. Phys. **32**, 1647–1659 (2005).

[29] M. Ferrant, S. K. Warfield, A. Nabavi, F. A. Jolesz, and R. Kikinis, “Registration of 3D Intraoperative MR Images of the Brain Using a Finite Element Biomechanical Model,” in *MICCAI*, Vol. 1935 Lecture Notes in Computer Science, 19−28 (Springer Verlag, Berlin/Heidelberg, 2000).

[30] P. Li, U. Malsch, and R. Bendl, “Combination of intensity-based image registration with 3D simulation in radiation therapy,” Phys. Med. Biol. **53**, 4621–4637 (2008).

[31] C. Tanner, J. A. Schnabel, D. L. G. Hill, D. J. Hawkes, M. O. Leach, and D. R. Hose, "Factors influencing the accuracy of biomechanical breast models," Med. Phys. **33**, 1758–1769 (2006).

[32] L. Han, J. Hipwell, T. Mertzanidou, T. Carter, M. Modat, S. Ourselin, and D. Hawkes, "A hybrid FEM-based method for aligning prone and supine images for image guided breast surgery," presented at 2011 IEEE International Symposium on Biomedical Imaging: From Nano to Macro, Chicago, IL, March 30−April 2, 2011.

[33] J. Liang and D. Yan, "Reducing and uncertainties in volumetric image based deformable organ registration," Med. Phys. **30**, 2116–2122 (2003).

[34] H. Zhong, J. Kim, H. Li, T. Nurushev, B. Movsas, and I. J. Chetty, "A finite element method to correct deformable image registration errors in low-contrast regions," Phys. Med. Biol. **57**, 3499–3515 (2012).

[35] J. A. Schnabel, C. Tanner, A. D. Castellano-Smith, A. Degenhard, M. O. Leach, D. R. Hose, D. L. G. Hill, and D. J. Hawkes, "Validation of nonrigid image registration using finite-element methods: Application to breast MR images," IEEE Trans. Med. Imaging **22**, 238−247 (2003).

[36] D. Mattes, D. R. Haynor, H. Vesselle, T. Lewellen, and W. Eubank, "Nonrigid multimodality image registration," Med. Imaging **4322**, 1609−1620 (2001).

[37] D. Mattes, D. R. Haynor, H. Vesselle, T. Lewellen, and W. Eubank, "PET-CT image registration in the chest using free-form deformations," IEEE Trans. Med. Imaging **22**, 120−128 (2003).

[38] M. Unser, A. Aldroubi, and M. Eden, "B-spline signal processing: Part I-Theory," IEEE Trans. Signal Process. **41**, 821−833 (1993).

[39] S. Klein, M. Staring, K. Murphy, M. A. Viergever, and J. P. W. Pluim, "Elastix: a toolbox for intensity based medical image registration," IEEE Trans. Med. Imaging **29**, 196–205, (2010).

[40] G. A. Holzapfel, *Nonlinear Solid Mechanics: A Continuum Approach for Engineering*, (John Wiley & Sons, Inc., 2000).

[41] J. C. Spall, "Implementation of the simultaneous perturbation algorithm of stochastic optimization," IEEE Trans. Aerosp. Electron. Syst. **34**, 817−823 (1998).

[42] P. H. Schönemann, "A generalized solution of the orthogonal Procrustes problem," Psychometrika **31**, 1−10 (1966).

[43] P. H. Ahn, A. I. Ahn, C. J. Lee, J. Shen, E. Miller, A. Lukaj, E. Milan, R. Yaparpalvi, S. Kalnicki, and M. K. Garg, "Random positional variation among the skull, mandible, and cervical spine with treatment progression during head-and-neck radiotherapy," Int. J. Radiat. Oncol., Biol., Phys. **73**, 626−633 (2009).

[44] L. Ibanez, W. Schroeder, and L. Ng, "The ITK software guide," Kitware Inc., www.itk.org (2003).

[45] J. R. Barber, *Elasticity*, 3rd ed. (Springer, Dordrecht, 2010).

[46] L. R. Dice, "Measures of the amount of ecologic association between species," Ecology **26**, 297–302 (1945).

[47] I. Gilad and M. Nissan M, "A study of vertebra and disc geometric relations of the human cervical and lumbar spine," Spine **11**, 154–157 (1986).

[48] Q. H. Zhang, E. C. Teo, H. W. Ng, and V. S. Lee, "Finite element analysis of moment-rotation relationships for human cervical spine," J. Biomech. **39**, 189–193 (2006).

[49] S. Hedenstierna and P. Halldin, "How does a three-dimensional continuum muscle model affect the kinematics and muscle strains of a finite element neck model compared to a discrete muscle model in rear-end, frontal, and lateral impacts," Spine **33**, E236−E245 (2008).

[50] J. V. Hajnal, N. Saeed, E. J. Soar, A. Oatridge, I. R. Young, and G. M. Bydder, "A registration and interpolation procedure for subvoxel matching of serially acquired MR images," J. Comput. Assist. Tomogr. **19**, 289−296 (1995).

[51] H. Wang, A. S. Garden, L. Zhang, X. Wei, A. Ahamad, D. A. Kuban, R. Komaki, J. O'Daniel, Y. Zhang, R. Mohan, and L. Dong, "Performance evaluation of an automatic anatomy segmentation algorithm on repeat or four-dimensional CT images using a deformable image registration method," Int. J. Radiat. Oncol., Biol., Phys. **72**, 210−219 (2008).